Check for updates

UV photodissociation and population dynamics of some important Criegee intermediates†

Behnam Nikoobakht, [ID] Maximilian F. S. J. Menger and Horst Köppel [ID] *

The influence of Criegee intermediates [CH_2OO, $(CH_3)_2COO$, *syn*- and *anti*-CH_3CH_2CHOO] on atmospheric chemistry depends significantly on their photodissociation dynamics under irradiation by sunlight. In this review, we highlight examples of electronic structure (multireference electronic wave functions) and nuclear quantum dynamics calculations relying on the wavepacket propagation technique for studying photodissociation dynamics of the Criegee intermediates in the visible or near UV region. In general, two interacting electronic states and three nuclear degrees of freedom are considered for construction of model Hamiltonians in our investigation. The UV absorption spectra are found to agree very well with available experimental recordings when accounting for broadening effects due to vibrational and rotational congestion and lifetime effects. This result serves to validate the Hamiltonian model built within the quasi-diabatic representation. It is found that the vibronic coupling is a vital ingredient to provide accurate insight into the photodissociation of these atmospheric species along the O−O bond and for reproducing the experimental absorption spectra, especially for the larger species $(CH_3)_2COO$, *syn*- and *anti*-CH_3CH_2CHOO. Time-dependent electronic populations reveal a faster decay than for the smaller system CH_2OO. This is interpreted in terms of the stronger coupling between the B and C states in the larger systems $(CH_3)_2COO$, *syn*- and *anti*-CH_3CH_2CHOO leading to the shorter lifetime for the B state compared to CH_2OO.

1 Introduction

In this review article, we concentrate on molecular species which are especially important for the Earth's lower atmosphere. These are in particular the carbonyl oxides or Criegee intermediates (CH_2OO, $(CH_3)_2COO$, *syn*- and *anti*-CH_3CH_2CHOO). Criegee intermediates, which constitute a significant fraction of volatile organic compounds in the Earth's atmosphere, originate from the ozonolysis of alkenes *via* carbonyl oxide intermediates.[1] Ozonolysis has been considered a well-known mechanism in the tropospheric oxidation of alkenes.[2–4] The ozonolysis reaction involves cycloaddition of ozone across the double bond of the alkene to constitute a primary ozonide, which is generated in a highly internally excited state and subsequently decays to a primary carbonyl species and a Criegee intermediate. Alkenes that perform atmospheric ozonolysis reactions can be categorized into two groups, *i.e.* those that are generated by vegetation in clean air environments and those that arise from anthropogenic sources in polluted environments.[5–7] Clean air environments tend to be richer in

alkenes such as terpenes and isoprenes. Ozonolysis of these larger alkenes produces semi-volatile oxygenated species that can finally generate secondary organic aerosols.[3] In urban areas, combustion emissions generate high levels of short chain alkenes including ethene, propene, butene, and pentene;[8] these unsaturated hydrocarbons are primary pollutants, accounting for about 12% of total volatile organic compounds.[8] These smaller alkenes are only slowly oxidized in atmospheric reactions with OH and O_3.[9,10] The Criegee intermediates produced from these smaller alkenes have 4 or less carbon atoms, starting with CH_2OO, $(CH_3)_2COO$ and CH_3CH_2CHOO, which are in the focus of this review, see Fig. 1.

In 1949 for the first time, Rudolf Criegee proposed that the "Criegee intermediates" are formed in the atmosphere during ozonolysis, the reaction of ozone O_3 with alkenes, or unsaturated hydrocarbons.[1,11] Criegee intermediates generated in this way are unstable and thus the direct measurements of the Criegee intermediates have been a challenge for a few decades.[1,12,13] To overcome this difficulty, it was suggested that one should generate directly Criegee intermediates in the laboratory and thus they do not elude direct detection.[1] One of the ways for its direct production in the gas phase (in the laboratory) relies on the role of iodine in the troposphere.[11,14–16] As suggested in these aforementioned references, a new synthetic method was used. In this method, they considered CH_2I_2 and used the photolysis process (which is the

Theoretische Chemie, Physikalisch-Chemisches Institut, Universität Heidelberg, INF 229, D-69120 Heidelberg, Germany. E-mail: horst.koeppel@pci.uni-heidelberg.de; Fax: +49 6221 545221; Tel: +49 6221 545214

† It is our pleasure to dedicate this paper to Prof. Christel Marian on the occasion of her 70th birthday.
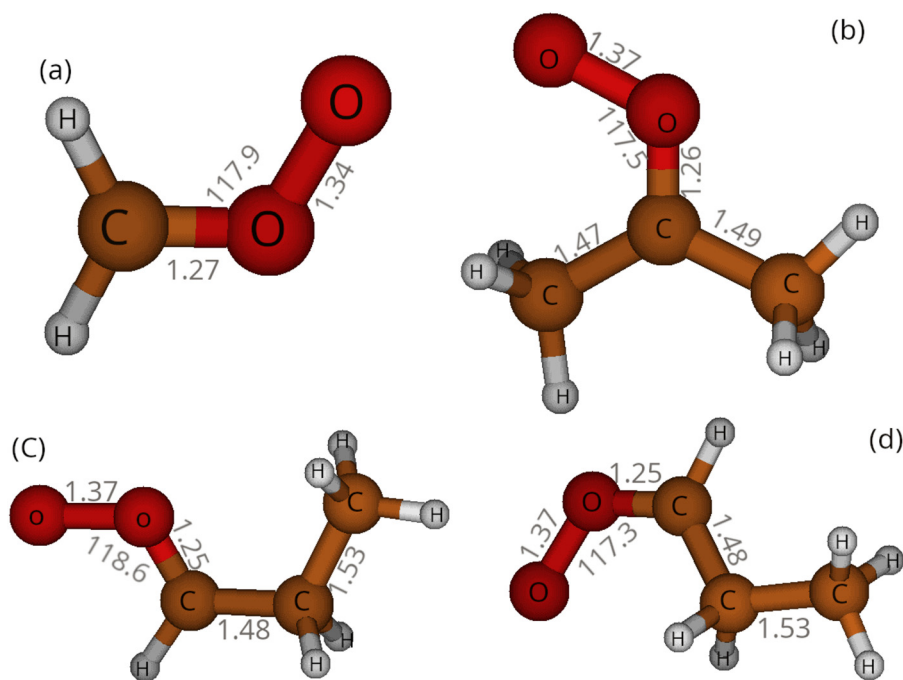
This journal is © the Owner Societies 2025

Phys. Chem. Chem. Phys., 2025, **27**, 20433–20452 | **20433**

Fig. 1 The ground state equilibrium structures of CH_2OO, $(CH_3)_2COO$, anti-CH_3CH_2CHOO and syn-CH_3CH_2CHOO shown in (a), (b), (c) and (d), respectively. The method UCCSD(T)-F12b/cc-pVTZ-F12 is used for CH_2OO, while for the other Criegee intermediates DFT/B3LYP is employed. For all atoms, the aug-cc-pVTZ basis set is used. The relevant bond lengths and angles are in Å and degrees, respectively.

dominant loss process in the atmosphere) to break one of the carbon–iodine bonds, then one can generate CH_2I and iodine[11,14–16]

$$CH_2I_2 + h\nu \rightarrow CH_2I + I. \quad (1)$$
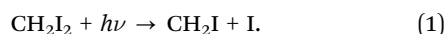
A Criegee intermediate is generated in the laboratory by the following reaction,

$$CH_2I + O_2 \rightarrow CH_2OO + I. \quad (2)$$

Direct studies, which have monitored the decay of a stabilized Criegee intermediate (SCI) or a proxy of the SCI (e.g. HCHO, OH), return rate coefficients that are considerably larger than previous indirect estimates based on end product analysis.[17] These new kinetic data suggest a greater role for SCI species in the atmospheric oxidation of SO_2 and NO_2 in particular. Field measurements support a role for the SCI assisted production of H_2SO_4[15] and although model studies disagree on the extent, they do agree that there is a non-negligible impact of Criegee intermediates on the oxidation of SO_2.[18] If the gas-phase oxidation of SO_2 to SO_3 (and subsequently H_2SO_4) by SCI competes with, or even dominates in regions of the lower troposphere, over the oxidation by OH, the formation of H_2SO_4 may be accelerated and aerosol nucleation rates be affected.[18]

$$CH_2OO + SO_2 \rightarrow HCHO + SO_3 \quad (3)$$

$$OH + SO_2 \rightarrow HOSO_2. \quad (4)$$
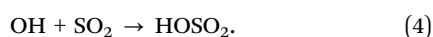
An experimental study was performed by using the Fourier-transform microwave spectroscopy technique providing valuable information about the electronic and geometric structure of CH_2OO.[19] The C–O bond length is close to that of a typical double bond and is shorter than that of the O–O bond. This argument proves that CH_2OO has a more zwitterionic character $H_2C = O^{\oplus}$–O, rather than a biradicaloid $H_2C^{\bullet}$–O–O$^{\bullet}$. For this molecule, the time-resolved UV absorption spectrum corresponding to the $B(^1A') \leftarrow X(^1A')$ electronic transition was measured.[20–23] The $B(^1A') \leftarrow X(^1A')$ transition of CH_2OO was assigned to an intense absorption band, and the confirming evidence for this assignment originated from chemical kinetic measurements of formation and decay time scales for this band.[20–22] CH_2OO was produced by using the reaction (2) and the authors measured the absorption spectrum within the wavelength range, 280–440 nm.[20,21] In the experimental work of Foreman et al., they reported room temperature spectrum of the $B(^1A') \leftarrow X(^1A')$ electronic absorption band of CH_2OO, acquired at higher resolution, using both single-pass broadband absorption and cavity ring-down spectroscopy. The new absorption spectra confirm the vibrational structure on the red edge of the band that is absent from ionization depletion measurements. They confirmed that the vibrational structure is not due to hot bands.[22]

In ref. 24, the potential energy surfaces (PESs) along O–O bond length corresponding to the electronic states X^1A', A^1A'' and B^1A' at the EOM-CCSD level using the 6-311++G(d,p) basis set were computed. They found that the B state is crossed near the Franck–Condon region by the C state potential surface. Due to this crossing it can be inferred that the dynamics after excitation to the B state depends on the strength of the

20434 | Phys. Chem. Chem. Phys., 2025, **27**, 20433–20452

This journal is © the Owner Societies 2025

interactions between these two B and C excited states. The precise determination of the coupling strength between these two states is important for a thorough understanding of the dynamics after excitation to the B state. This coupling can be zero, weak or strong. Zero coupling between the two states C and B would produce bound, potentially fluorescent vibrational levels in the B state. Weak coupling between these two states would result in predissociation of the B and C states, with potential for vibrational structure in the spectrum. Strong coupling would cause these two C and B states to avoid each other (repel) significantly in the vicinity of the crossing point. Lee *et al.* simulated the absorption spectrum using the double-harmonic approximation.[25] However, anharmonicity was not taken into account; consequently no agreement between their simulation and the latest experimental results was achieved (see ref. 21). Dawes *et al.* computed the absorption spectrum corresponding to the $B(^1A') \leftarrow X(^1A')$ electronic transition using the Chebyshev real wave packet method, where they used the 1D model Hamiltonian depending on only the O–O stretching coordinate and obtained a spectrum in good agreement with the corresponding experimental one.[26] However, they were not able to produce the vibronic structure appearing in the experimental spectrum and neither the considerable shift between the computed and experimental spectra specially at longer wavelengths. In the experimental work of Chhantyal-Pun *et al.*,[27] the authors reported that CH_2OO oxidizes SO_2 to SO_3 and hence may contribute to atmospheric sulphuric acid production. They measured the bimolecular reaction rate of $CH_2OO + SO_2$ under low pressure and ambient temperature conditions *via* direct study. These authors measured a rate coefficient of $(3.80 \pm 0.04) \times 10^{-11}$ cm^3 $molecule^{-1}$ s^{-1} for the reaction of $CH_2OO + SO_2$ at low SO_2 concentrations. They mentioned that at low SO_2 concentrations, the formation of the triplet state in the biradical adduct of CH_2OO and SO_2 *via* intersystem crossing (ISC) may play an important role in the reaction of $CH_2OO + SO_2$. Other theoretical investigations showed that there is a small difference between the singlet and triplet states (0.4 kJ mol^{-1}).[12,13]

Regarding larger Criegee intermediates, $(CH_3)_2COO$, as well as its structural isomer CH_3CH_2CHOO were generated by synthesizing of $(CH_3)_2CI_2$ and $(CH_3)CH_2CHI_2$ precursors, respectively in the laboratory.[28] Experimental evidence showed that these species have a more zwitterionic character rather than a biradicaloid nature.[28] The authors of ref. 28 and 29 measured the absorption spectra corresponding to the $\tilde{B}(^1A') \leftarrow \tilde{X}(^1A')$ electronic transition for these species in the wavelength range 280–380 nm. In ref. 29, authors also computed the spectrum and observed a good agreement between the theoretical and experimental spectra for $(CH_3)_2COO$. Authors in ref. 28 observed the significant depletions of the ion signals when UV laser radiations with wavelengths near the peak of the absorption spectrum (323 and 322 nm for $(CH_3)_2COO$ and CH_3CH_2CHOO, respectively) are introduced prior to the VUV photoionization laser. They argued that these large depletions are indicative of rapid dynamics in the excited B state, most likely due to direct dissociation.[28]

Motivated by these studies, we have investigated the photo-dissociation dynamics and UV absorption spectra of the Criegee intermediates mentioned above.[30–33] We have primarily focused on two aspects. First, the PESs of the excited states with A′ symmetry are studied by employing multireference methods, and thus the role of electron correlation is taken into account by selecting a suitable active space. This is followed by constructing model Hamiltonians for each molecule in which the vibronic coupling between PESs of the two lowest excited A′ states is estimated by the minimum energy difference at the avoided crossing geometries. Second, the photodissociation dynamics is studied by employing a fully quantal description of the nuclear motion using the model Hamiltonians built in the first step and the multiconfiguration time-dependent Hartree (MCTDH) approach.[34–37] As will be mentioned, this results in computed spectra and time-dependent populations of the electronic states of each molecular species involved in the dynamics. This analysis can provide an accurate and quantitative innht into the photodissociation dynamics of these important atmospheric molecules under irradiation by sunlight.[30–33,38]

In the following section (Section 2), the detailed information regarding the construction of the Hamiltonian model will be addressed. In Section 3, the diabatization by ansatz method adopted will be introduced. In Section 4, the details of electronic structure methods for computing optimized geometries, and potential energy surfaces (PESs) will be outlined. Section 5 is devoted to the discussion of the absorption spectra of each molecular species, where they are compared with available experimental spectra. The time-dependent population analysis is documented in Section 6. Finally, Section 8 is devoted to summary and outlook.

2 Vibronic Hamiltonian and quantum dynamical approach

In our previous works,[31–33] vibronic model Hamiltonians for the description of the UV absorption process for these Criegee intermediates were suggested. These models yield a good agreement between the computed spectra and the corresponding experimental ones indicating that the models can express reliably the physical processes underlying the UV absorption spectroscopy and ultrafast radiationless decay. Here, we recap the main idea for the construction of the model Hamiltonian for these molecular species. The vibronic Hamiltonian H is constructed in a (quasi-)diabatic electronic basis (see *e.g.* ref. 37 and 39) for the B^1A' and C^1A' states of the Criegee intermediates, while the X^1A' state is assumed to be decoupled in the usual adiabatic picture,

$$H = T_N \mathbf{1} + W(S). \tag{5}$$

Here H contains the kinetic part T_N ($\mathbf{1}$ stands for the 3×3 unit matrix) and the potential part $W(S)$. As we showed previously for the relevant Criegee intermediates,[31–33] a 3D Hamiltonian model including the O–O, C–O stretching and C–O–O

bending modes is sufficient to produce the UV absorption spectra in a very satisfactory agreement with the corresponding experimental results. The Hamiltonian model includes the O–O and C–O stretching and the C–O–O bending modes. The three modes are totally symmetric, *i.e.* of a′ symmetry for planar conformations (C_s point group). In the diabatic representation for the excited states, $W(S)$ reads

$$W(S) = \begin{pmatrix} V_X(S) & 0 & 0 \\ 0 & W_B(S) & W_{BC}(S) \\ 0 & W_{BC}(S) & W_C(S) \end{pmatrix}. \qquad (6)$$

In eqn (6), the vector S refers to the three relevant internal coordinates mentioned above. $V_X(S)$ refers to the adiabatic PES for the ground state X^1A', while $W_B(S)$ and $W_C(S)$ correspond to the PESs of the relevant B^1A' and C^1A' electronic states in the diabatic representation along the relevant internal coordinates. $W_{BC}(S)$ is the potential coupling between the B and C states. It is known that these Criegee intermediates are dissociated *via* the O–O bond cleavage in the presence of UV light (see Section 4). Since in the wavepacket (WP) propagation calculation, we need to consider periodic boundary conditions (*e.g.* FFT), the WP along the O–O stretching coordinate can be reflected or it penetrates the other side of the grid leading to the depreciation of the wavefunction. A complex absorbing potential (CAP) along the O–O stretching coordinate will be used in the model Hamiltonian of eqn (6) to avoid the convergence issue in the WP propagation calculation. This includes an negative imaginary potential (introduced by Leforestier and Wyatt,[40] and later Kosloff[41]), which is used to absorb the wavepacket as it approaches the end of the grid. It thus helps in the propagation to converge better along the O–O stretching coordinate. The CAP is usually defined as follows[35]

$$iW(Q) = -i\eta(Q - Q_c)^b \theta(Q - Q_c) \qquad (7)$$

In this equation, Q_c, b and η are the starting point, order, and strength of the CAP, respectively. The parameters Q_c, η and b used in the current work are 2.1 Å, 3.1×10^{-4} a.u., 3, respectively.[30–33] The symbol $\theta(x)$ refers to Heaviside's step function. The distance between the starting point of the CAP and the end of the grid determines the length of the CAP, which is usually specified by visualizing the topology of potential energy cuts (see Section 4). The optimal CAP order is 2 or 3 as suggested in ref. 42. In our study, the length of the CAP is $\sim$1.4, resulting in a sufficiently smaller CAP strength η to avoid unwanted CAP reflections in the quantum dynamical calculation (see ref. 42 for more information for determining of the CAP parameters). We thus modify the potential part of the Hamiltonian in eqn (6) by adding $iW(Q)$ according to eqn (7).

We compute the kinetic part T_N of the Hamiltonian using the familiar G-matrix method of Wilson *et al.*[43,44] as indicated in our previous works.[31–33] Since we are considering the O–O stretch, C–O–O bend and C–O stretch in the evaluation of $W(S)$ in eqn (6), the C and O atoms play roles in the evaluation of the kinetic operator. Thus, the kinetic operator reads,[30,43]

$$\begin{aligned} T_N = &-\mu_O \frac{\partial^2}{\partial R^2} + \frac{1}{2}\rho_{CO}\mu_O \sin\theta \frac{\partial^2}{\partial R \partial \theta} \\ &-\frac{1}{2}(\rho_{OO}^2\mu_O + \rho_{CO}^2\mu_C)\frac{\partial^2}{\partial \theta^2} \\ &-\frac{1}{2}(\rho_{OO}^2 + \rho_{CO}^2)\mu_O \frac{\partial^2}{\partial \theta^2} \\ &+\rho_{OO}\rho_{CO}\mu_O \cos\theta \frac{\partial^2}{\partial \theta^2} - \frac{1}{2}(\mu_C + \mu_O)\frac{\partial^2}{\partial R'^2} \\ &-\frac{1}{2}\mu_O \cos\theta \frac{\partial^2}{\partial R \partial R'} \\ &+\frac{1}{2}\rho_{OO}\mu_O \sin\theta \frac{\partial^2}{\partial R' \partial \theta}. \end{aligned} \qquad (8)$$

The variables R, R' and θ refer to the O–O and C–O stretching as well as C–O–O bending coordinates, respectively. In eqn (8), the coefficients are defined as follows,

$$\mu_O = 1/m_O \quad \mu_C = 1/m_C \quad \rho_{OO} = 1/R_{OO} \quad \rho_{CO} = 1/R_{CO}, \qquad (9)$$

where $m_O = 15.999$ and $m_C = 12.011$ in atomic mass units. For the R_{OO} and R_{CO} stretching coordinates and the θ_{COO} bending coordinate, we use the values for the ground state equilibrium structure of the Criegee intermediates shown in Fig. 1.

We use the multi-configuration time-dependent Hartree (MCTDH) method[34–36] for the nuclear quantum dynamics calculations. More detailed information regarding the MCTDH approach can be found in the literature (*e.g.* ref. 34–36). The relevant information as employed in this work is given in our previous papers[30,31] and thus we skip it in the current work. We use the POTFIT method for fitting the *ab initio* data to the model introduced in eqn (6). We refer the reader to ref. 31 for more details relevant to this aspect. For more details on the POTFIT method, the reader is referred to ref. 45.

3 Diabatization of excited-state potential energy surfaces

It is well known that the Born–Oppenheimer separation of electronic and nuclear motions fails when two or more electronic states are close in energy within a certain range of the nuclear coordinate space.[46] Within this condition, the Born–Oppenheimer approximation can be still used if one can develop an efficient method to deal with the near-degeneracy of electronic states in localized regions of coordinate space. A suitable choice to circumvent this issue is the introduction of suitable "diabatic" electronic states that may cross as a function of the internuclear distances, whereas the adiabatic electronic states are subject to the noncrossing rule.[37,39,47–49] There are a number of ways to diabatize the adiabatic PESs (*e.g.* regularized diabatic states).[50,51]

For the purpose of the excited-state PES diabatization of these Criegee intermediates, we have used a diabatization-by-ansatz

20436 | *Phys. Chem. Chem. Phys.*, 2025, **27**, 20433–20452
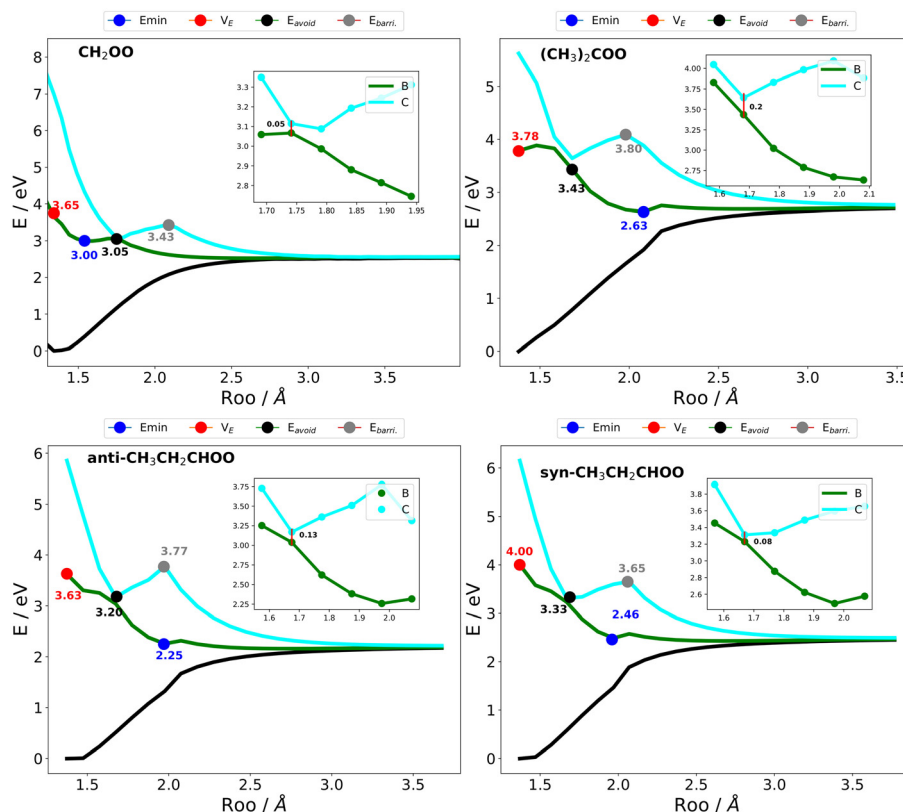
This journal is © the Owner Societies 2025

Fig. 2 Adiabatic PECs of the Criegee intermediates along the O–O bond length for the three states X^1A' (black), B^1A' (green) and C^1A' (cyan). The vertical excitation energy, minimum energy of the B state, energy at the avoided crossing and the energy at the barrier maximum are shown by red, blue, black and gray circles, respectively. In the insets, the energy gaps at the avoided crossing geometries are shown. The other molecular coordinates are fixed at the equilibrium structure values.

approach.[30–33] This is a well-known method in the diabatization context and well developed in the literature.[37,39] For the Criegee intermediates discussed in this study, the relevant excited states are B^1A' and C^1A' and the relevant coordinate is the O–O distance, that is a single nuclear coordinate. Illustrations are provided by Fig. 2 (see also Section IV for the *abinitio* methods adopted).

We apply the diabatization-by-ansatz approach in the spirit of the well-established vibronic coupling model where only the coupling terms of leading order are retained. For such one-dimensional same-symmetry problems the leading coupling terms are of order R_{OO}^0 or constant. This allows to extract the diabatic potentials in a simple way from the adiabatic quantities by equating the off-diagonal coupling W_{BC} with the minimum energy gap along the avoided crossing, as follows.

Diagonalizing the block of the potential matrix in eqn (6) results in the energies of the B^1A' and C^1A' states in the adiabatic picture. The diagonalization of each block can be represented as follows:

$$U_{ij}(\boldsymbol{S})^{\dagger} \begin{pmatrix} W_i(\boldsymbol{S}) & W_{ij}(\boldsymbol{S}) \\ W_{ij}(\boldsymbol{S}) & W_j(\boldsymbol{S}) \end{pmatrix} U_{ij}(\boldsymbol{S}) = \begin{pmatrix} V_i(\boldsymbol{S}) & 0 \\ 0 & V_j(\boldsymbol{S}) \end{pmatrix}, \quad (10)$$

where $i \in \{B^1A'\}$ and $j \in \{C^1A'\}$. The off-diagonal term $W_{ij}(\boldsymbol{S})$ refers to the vibronic coupling between the coupled states (B^1A', C^1A') and is shown as $W_{BC}(\boldsymbol{S})$, in the Hamiltonian model. In this equation, $\boldsymbol{U}_{ij}(\boldsymbol{S})$ is a unitary transformation and reads

$$\boldsymbol{U}(\boldsymbol{S}) = \begin{pmatrix} U_{ii}(\boldsymbol{S}) & U_{ij}(\boldsymbol{S}) \\ U_{ji}(\boldsymbol{S}) & U_{jj}(\boldsymbol{S}) \end{pmatrix} = \begin{pmatrix} \cos(\alpha_{ij}(\boldsymbol{S})) & \sin(\alpha_{ij}(\boldsymbol{S})) \\ -\sin(\alpha_{ij}(\boldsymbol{S})) & \cos(\alpha_{ij}(\boldsymbol{S})) \end{pmatrix}, \quad (11)$$

where $\alpha(\boldsymbol{S})$ is the adiabatic to diabatic (ATD) transformation angle and given by

$$\alpha_{ij}(\boldsymbol{S}) = \frac{1}{2}\arctan\frac{2W_{ij}(\boldsymbol{S})}{W_i(\boldsymbol{S}) - W_j(\boldsymbol{S})}. \quad (12)$$

We define the matrix elements of the unitary transformation using the sin and cosine functions depending on the ATD angle (see eqn (11) and (12)). Taking the eigenvalue problem in eqn (10) to be solved, we compute the diabatic PESs in terms of adiabatic energies $V_i(\boldsymbol{S})$ and $V_j(\boldsymbol{S})$ obtained from the electronic structure methods discussed in the next section. Thus, the diabatized surfaces can be computed using the

This journal is © the Owner Societies 2025

Phys. Chem. Chem. Phys., 2025, **27**, 20433–20452 | **20437**

following relations,

$$W_B(S) = \frac{V_B(S) + V_C(S)}{2} - \sqrt{\left(\frac{V_B(S) - V_C(S)}{2}\right)^2 - W_{BC}^2}$$

$$W_C(S) = \frac{V_B(S) + V_C(S)}{2} + \sqrt{\left(\frac{V_B(S) - V_C(S)}{2}\right)^2 - W_{BC}^2}.$$

$$(13)$$

The diabatic energies $W_{B,C}$ can thus be obtained from the adiabatic counterparts $V_{B,C}$ once the quantity W_{BC} is known. This is determined from the minimum energy difference between states B and C, see next section.

4 Quantum chemistry methods and potential energy surfaces

We used the optimized structures reported in the previous works.[30,32,33] The UCCSD(T)-F12b/cc-pVTZ-F12 level of theory was employed for the optimization of the CH_2OO ground state structure,[52,53] while the semiempirical density functional theory (DFT) method with the B3LYP functional[54,55] and the aug-cc-pVTZ basis set for all atoms[53] was used for the $(CH_3)_2COO$ and CH_3CH_2CHOO molecules. The resulting equilibrium ground state structures of for these molecular systems are shown in Fig. 1.

For the CH_2OO, the potential energy surfaces (PESs) were computed in our previous work[31] by employing the CASPT2-F12 (hereafter RS2-F12)[52] method using the cc-pVTZ-F12 basis set for all atoms.[53,56] We employ the full-valence complete active space (CAS), with 18 electrons distributed in 14 orbitals (18e,14o). For $(CH_3)_2COO$ molecule and CH_3CH_2CHOO with its molecular conformers,[32,33] we used the RS2C method (second-order multireference perturbation theory with a more contracted configuration space)[57] with the basis set 6-311++G(2d,2p) for all atoms.[58] For this calculation, the active space with eight electrons distributed in eleven orbitals, CAS(8e,11o), is employed. During the evaluation of the PESs, state averaging is used in order to avoid root-flipping problems. In the state averaging, we consider the three lowest states of a′ symmetry and the two lowest states of a″ symmetry. For all molecules, we compute the PESs along R_{OO}, θ_{COO} and R_{CO} for the X^1A', B^1A' and C^1A' states within the ranges specified in Table 1. For the evaluation of PESs along the relevant coordinates, we keep the other coordinates fixed at the equilibrium values mentioned in Fig. 1. The geometry optimizations and PES computations are carried out by using the MOLPRO 2019.2

Table 2 Reported vertical excitation energies of the B and C states and their character for the relevant Criegee intermediates in this work. The corresponding reference for each value is mentioned in the table footnote

Molecule	Transition	Theory	Experiment
CH_2OO	$\pi \to \pi^*$	3.66^a, 3.83^b, 3.65^c, 3.81^d, 3.75^e, 4^f	3.65^a, 3.704^f
	$n \to \sigma^*$	6.99^c	—
$(CH_3)_2COO$	$\pi \to \pi^*$	3.78^g, 3.82^h	3.82^h
	$n \to \sigma^*$	5.62^g	—
syn-CH_3CH_2CHOO	$\pi \to \pi^*$	4.00^j	3.85^i
	$n \to \sigma^*$	6.15^j	—
$anti$-CH_3CH_2CHOO	$\pi \to \pi^*$	3.63^j	—
	$n \to \sigma^*$	5.85^j	—

^{a} Ref. 22. ^{b} Ref. 30. ^{c} Ref. 31. ^{d} Ref. 60. ^{e} Ref. 26. ^{f} Ref. 20. ^{g} Ref. 32. ^{h} Ref. 61. ^{i} Ref. 28. ^{j} Ref. 33.

suite of programs.[59] In Fig. 2, the adiabatic potential energy cuts (PECs) along R_{OO} by fixing all other coordinates, for the X (black line), B (green line) and C (cyan line) states are shown for all Criegee intermediates relevant to this work.[31–33] It can be seen that the PECs of B and C states represent avoided crossings for all four cases shown in this figure. The avoided crossings for CH_2OO, $(CH_3)_2COO$, syn-CH_3CH_2CHOO and $anti$-CH_3CH_2CHOO occur at 3.05, 3.43, 3.20, 3.33 eV, respectively, while locations of the avoided crossing along R_{OO} are 1.74, 1.68, 1.66 and 1.67 Å, respectively. The vertical excitation energies of the B states are indicated by red circles in each panel. We also compare our values with the available ones in the literature (see Table 2). For all molecular cases, in the asymptotic limit of O–O stretch, CH_2OO, $(CH_3)_2COO$ and syn- and $anti$-CH_3CH_2CHOO are dissociated via the O–O bond cleavage to $H_2CO(X^1A)$ + $O(^1D)$, $(CH_3)_2CO$ + $O(^1D)$ and CH_3CH_2CHO + $O(^1D)$ products, respectively. The estimated dissociation energies for these Criegee intermediates are 2.55, 2.76, 2.22 and 2.49 eV, respectively.

It can be seen that the minimum energy of the B state (shown by blue color circle in each panel of Fig. 2) for CH_2OO is located slightly before the avoided crossing while for the rest of Criegee intermediates it is after the avoided crossing. In the inset of each panel in Fig. 2, the PECs for the B and C states are replotted in a smaller energy range allowing to observe clearly the energy gap between the minimum energies of each curve. This indicates that it has the smallest value for CH_2OO (0.05 eV) and the largest value for $(CH_3)_2COO$ (0.2 eV). Thus, for the specific PECs shown in Fig. 2, one may conclude that the PECs of the B and C states are more strongly avoided in the case of $(CH_3)_2COO$ compared with other Criegee intermediates.

In Fig. 3, we plot – for R_{CO} fixed at the ground state equilibrium – the minimum energy difference between the B and the C state along the R_{OO} stretching coordinate for various

Table 1 The grid used for molecular coordinates of all Criegee intermediates

Molecule	R_{OO}	Interval	θ_{COO}	Interval	R_{CO}	Interval
CH_2OO	1.09–4.0 Å	0.05 Å	92°–120°	2°	1.12–1.32 Å	0.05 Å
$(CH_3)_2COO$	1.38–3.48 Å	0.1 Å	102°–120°	2°	1.06–1.46 Å	0.1 Å
syn-CH_3CH_2CHOO	1.30–4.0 Å	0.1 Å	110°–122°	2°	1.16–1.46 Å	0.1 Å
$anti$-CH_3CH_2CHOO	1.30–4.0 Å	0.1 Å	110°–124°	2°	1.15–1.45 Å	0.1 Å

20438 | *Phys. Chem. Chem. Phys.*, 2025, **27**, 20433–20452
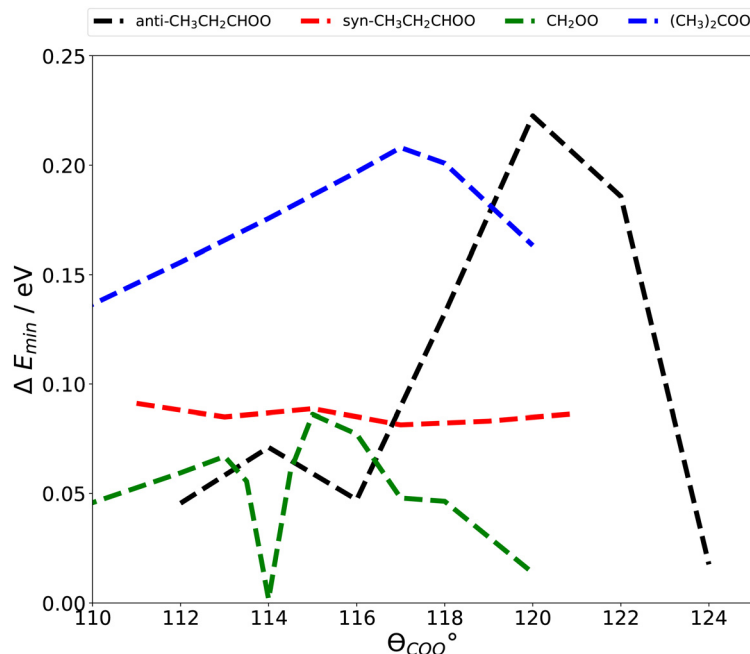
This journal is © the Owner Societies 2025

Fig. 3 Minimum energy difference of the R_{OO} PE curves of the B and C states for all Criegee intermediates. The dependence of the minimum energy difference on θ_{COO} is taken into account by carrying out the calculation for different values of θ_{COO} in the range of $110° < \theta_{COO} < 124°$. In this figure, the values of R_{CO} for each molecule are fixed at their ground state equilibrium structures specified in Fig. 1.

values of θ_{COO}. This is done for the various Criegee intermediates. Afterwards we average over θ_{COO} and repeat this procedure for different values of R_{CO}, as shown in Fig. 4a. An overview of the selected values for R_{CO} and R_{OO} is presented in Table 1. Finally we average over R_{CO} to get the average values $\widetilde{\Delta E}_{\theta,R_{CO}}$ presented in Fig. 4b for the various Criegee intermediates. This is equated with twice the off-diagonal potential coupling W_{BC}. Thus, within this 3D PESs, *anti*-CH$_3$CH$_2$CHOO shows the largest vibronic coupling between the B and the C state indicating that the B and the C state show a stronger repulsion compared with the other Criegee intermediates. Please note that this finding is not the same as the one in Fig. 2, where the PECs of B and C state are computed only along R_{OO}.

In the following, the PECs are diabatized based on the method described in Section 3. In a one-dimensional treatment the coupling W_{BC} is assumed to be constant (as indicated above). The other degrees of freedome θ_{COO} and R_{CO} are treated as spectator modes and are accounted for by the simple averaging procedure described above, thus modifying the constant coupling W_{BC}. The resulting diabatic PECs are shown in Fig. 5. The use of a diabatic representation is a consequence of the weakly avoided crossing between the B^1A' and C^1A' adiabatic states. Due to the nature of the diabatization process, the diabatic PECs are smoother than the corresponding adiabatic ones in Fig. 2. Thus, as can be seen in Fig. 2 and 5, changing the avoided crossing features to intersection points is a consequence of the diabatization process removing potential couplings between the adiabatic states. Within these diabatized PESs, we can estimate the barrier energy of the B state for each molecule. Fig. 5 shows that barrier heights of 0.38, 0.01, 0.57

and 0.32 eV are estimated for CH$_2$OO, (CH$_3$)$_2$COO, *syn*-CH$_3$CH$_2$CHOO and *anti*-CH$_3$CH$_2$CHOO, respectively.

In Fig. 5, the imaginary part of the complex absorption potential (CAP) along the O–O stretching coordinate relevant to the photodissociation along this coordinate is also included. The CAP starts at ~2.11 Å, right after the barrier of the diabatic B state.

5 Absorption spectroscopy

5.1 CH$_2$OO

The absorption spectroscopy of CH$_2$OO has been studied experimentally and theoretically since a decade ago.[20–22,24,28,62–64] The early measurements have been carried out by Lester and co-workers, who reported the action spectra corresponding to the Criegee intermediates and identified a very strong UV absorption of CH$_2$OO, due to the B ← X transition within the UV region.[20] The velocity and angular distributions of O(^{1}D) photofragments arising from UV excitation of CH$_2$OO by the $B^1A' ← X^1A'$ transition indicate that the corresponding electronic transition has $\pi^* ← \pi$ character.[62] Sheps also measured the $B^1A' ← X^1A'$ electronic transition of formaldehyde oxide, CH$_2$OO, produced by the reaction of CH$_2$I radicals with O$_2$.[21] In contrast to its UV photodissociation action spectrum, the absorption spectrum of formaldehyde oxide extends to longer wavelengths and exhibits resolved vibrational structure on its low-energy side.[21] In another attempt carried out by Foreman *et al.*, a high-resolution absorption spectrum of CH$_2$OO was reported in which the authors confirmed the presence of vibrational structure on the red edge of the band for the first time.[22] There have been significant discrepancies among the
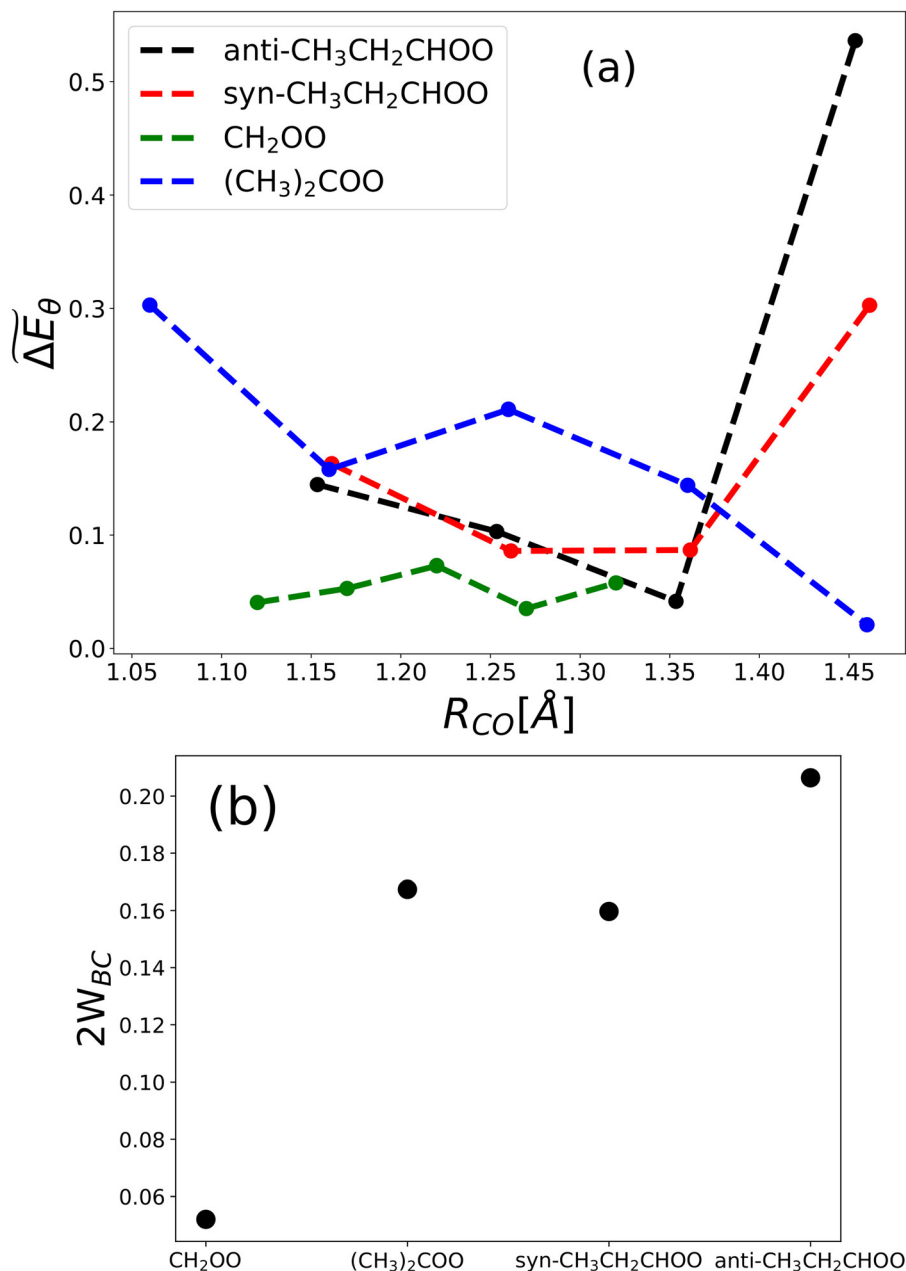
This journal is © the Owner Societies 2025

Phys. Chem. Chem. Phys., 2025, **27**, 20433–20452 | **20439**

Fig. 4 (a) $\widetilde{\Delta E_\theta}$ (average of the minimum energy difference $\Delta E_{\min}$ over the bending angle for all Criegee intermediates) in terms of R_{CO} within the molecular coordinate range specified in Table 1. (b) The black dots refer to the average of $\widetilde{\Delta E_\theta}$ over the range of R_{CO} specified in Table 1 for each molecule. These doubly averaged values $\widetilde{\Delta E_{\theta,R_{CO}}}$ are used as twice the coupling constants between the B and C states or twice the off-diagonal element W_{BC} in the 3D model for all Criegee intermediates.

reported measurements of the strong B^1A'–X^1A' electronic transition in the visible/near-UV spectral range. The peak cross section measured by Ting et al. is $(1.23 \pm 0.18) \times 10^{-17}$ cm^2 at 340 nm.[23] This number is significantly smaller than the previous values reported e.g. by Sheps.[21] Ting et al. mentioned that this intense B^1A'–X^1A' excitation spectrum overlaps with the incoming solar spectrum, thus yielding efficient photolysis of CH$_2$OO.[23] Furthermore, the reported spectrum by Ting et al. shows stronger vibrational structures in the long-wavelength range ($\lambda > 360$ nm) compared with Sheps' work. Foreman et al.[22] performed a similar

measurement and their result gave significant vibrational structure in the low-energy part of the B^1A'–X^1A' excitation spectrum of CH$_2$OO.

In ref. 30 and 31, we have also focused on the photodissociation dynamics of CH$_2$OO using the nuclear quantum dynamics approach (see Table 3). We performed a quantum dynamical calculation considering three vibrational modes, the R_{OO} and R_{CO} stretching modes as well as the θ_{COO} bending mode, where the PESs corresponding to the X, B and C states were computed by using the MRCI-F12 and RS2-F12 methods as
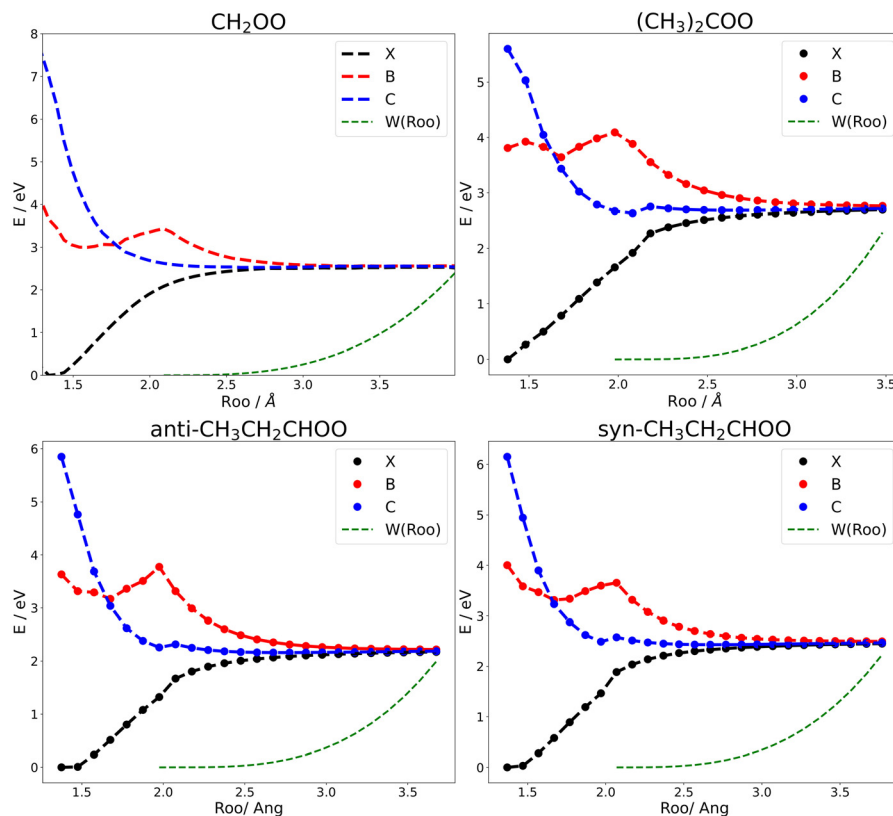
20440 | Phys. Chem. Chem. Phys., 2025, **27**, 20433–20452

This journal is © the Owner Societies 2025

Fig. 5 Diabatic PECs of the B and C states as function of R_{OO} obtained by employing the diabatization by ansatz method. The dashed green lines refer to the CAP as defined by using eqn (7). It is used in the diagonal elements of the model Hamiltonian of eqn (6) to let the propagation calculation converge faster along the O–O stretching coordinates for all Criegee intermediates.

Table 3 Number of basis functions for the primitive harmonic and SPF basis used for the propagation calculations

Modes	DVR	Primitive basis	SPF basis
R_{OO}	FFT	128	9, 10, 9
R_{CO}	HO	88	9, 10, 9
θ_{COO}	HO	80	9, 10, 9

mentioned in Section 4. The coupling between the B and C states was taking into account in our Hamiltonian model. We used the Hamiltonian of eqn (5) in the propagation calculation and computed the absorption spectrum within different wavelength ranges. In Fig. 6, we present the B^1A'–X^1A' excitation spectrum of CH_2OO computed using the 3D model including the O–O and C–O stretching as well as C–O–O bending modes (shown by the solid green line in Fig. 6). The corresponding PESs were computed by using the RS-F12 method.[30] In this figure, we also present the absorption spectrum (shown by the solid blue line in Fig. 6) obtained by using the 2D PESs depending on the O–O stretching and C–O–O bending coordinates. These 2D PESs were evaluated by employing the MRCI-F12b method.[30] We further compared our results for CH_2OO with the available theoretical results in the literature.[26,30] The dark blue line in Fig. 6 was computed in our previous work using the 2D model (depending only on
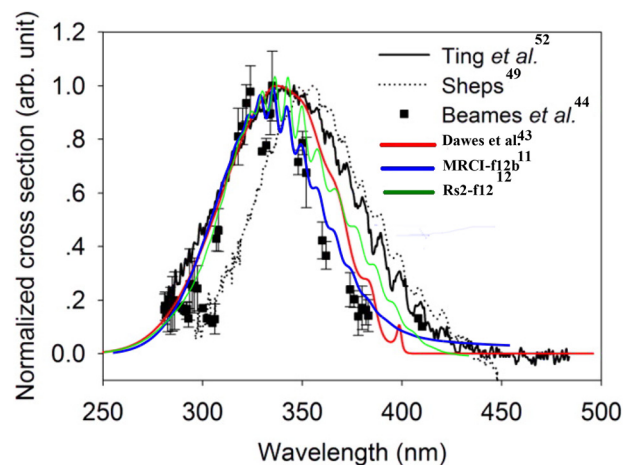

Fig. 6 The computed excitation spectrum of CH_2OO for the B^1A'–X^1A' transition compared with the available experimental and theoretical results from ref. 20, 21, 23 and 26, respectively. The dark blue line is taken from our previous work,[30] based on the 2D PES using MRCI-F12 method. The full green line (this work) is obtained from the 3D model (r_{OO}, r_{CO} and θ_{COO}) based on the RS2-F12 method.

the r_{OO} and θ_{COO} coordinates) with PESs evaluated by the MRCI-F12b method,[30] while the solid red line was calculated by Dawes et al.,[26] who used a 1D model with the uncoupled

This journal is © the Owner Societies 2025

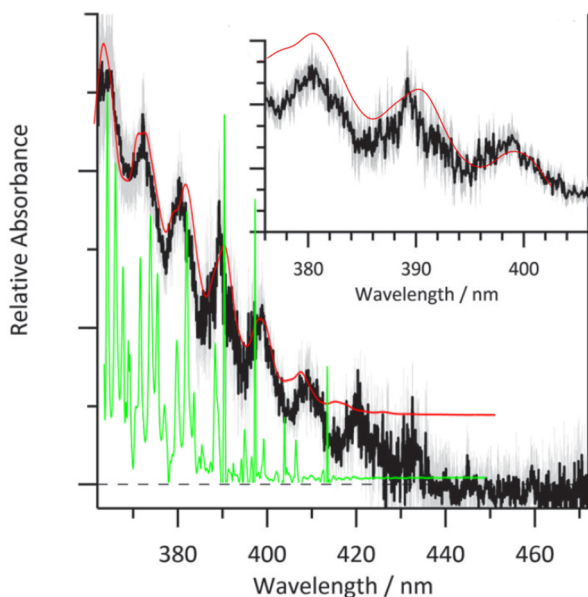*Phys. Chem. Chem. Phys.*, 2025, **27**, 20433–20452 | **20441**

Fig. 7 Comparison of the computed low-energy part of the excitation spectrum employing the 3D model using the RS2-F12 method with the experiment from ref. 22. The spectrum with green color has no dephasing time, while the spectrum depicted in red has a dephasing time $\tau = 40$ fs (also in inset), which depicts the spectrum on an expanded scale.

observed vibrational progressions to the excitation of bound levels of the B state, while it was mentioned in ref. 28 that the progressions originate from hot bands.[28] To further investigate on the low energy part of the absorption spectrum ($\lambda > 360$ nm), we set up comprehensive nuclear quantum dynamical calculations in ref. 31, in which we carried out propagation calculations employing the 3D, 2D and 1D model Hamiltonians. In Fig. 7, the spectra evaluated with dephasing times 40 and 1000 fs are depicted by red and green lines, respectively, and compared with experiment. In the inset, the spectrum within the wavelength range of 376–406 nm is visualized (red line) and compared with the experimental spectrum measured by Foreman *et al.* in ref. 22 (black line). From this result, one can see that the positions of observed peaks are very well reproduced by the 3D calculation, and thus an excellent agreement between theory and experiment is achieved. In ref. 31, we further investigated the aboosorption spectrum using the 2D and 1D model diabatic PES depending the O–O stretching and C–O–O bending coordinates. Detailed nuclear quantum dynamical calculations from these calculations revealed that the main spectral progression represents the O–O stretching and C–O–O bending modes.[31]

So far, we have treated the B and C states are coupled states. The question arises, whether the vibronic coupling plays an important role in reproducing the spectrum or not. To address it, we compute the spectrum using the uncoupled 1D, 2D and 3D models separately. The corresponding results are shown in Fig. 8. Although not directly visible from the figures, a closer analysis reveals that the coupled and uncoupled 3D spectra are crudely similar in the appropriate energy range. Thus, the vibronic coupling plays a less important role in the spectrum. In Fig. 8, it can be seen that the computed spectrum shows quasi-discrete and continuous features below and above the barrier energies (E_b) of the diabatic B state, respectively using the 1D, 2D and 3D model Hamiltonians. Furthermore, increasing the dimensiality in the Hamiltonian models shifts the energy barrier of the diabatic B state towards the high-energy part of the $B^1A' \leftarrow X^1A'$ absorption spectrum. As a result, we can observe more quasi-discrete structure in the spectrum obtained from the 3D model than in the spectra obtained *via* the 2D and 1D models. In principle, the continuous part of the spectrum within the 3D model is located in the spectrum tail beyond ~4 eV.
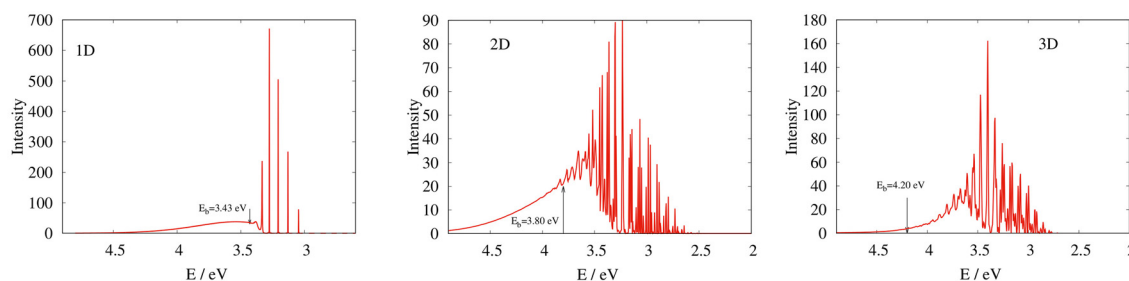
adiabatic PES of the B state alone as a function of the O–O stretching coordinate. The dephasing time in the spectrum shown by dark blue and green lines is 22 fs. It can be seen that there is agreement between the green line spectrum and the experimental result of Ting *et al.*, see Fig. 6. In fact, the main peak of both spectra occurs at ~3.65 eV (or 339 nm) and the shape of the computed spectrum is close to the experimental result of the Ting *et al.* especially for $\lambda < 340$ nm. Another important feature of the green line spectrum is that it produces nicely the vibronic structures in the low-energy part of the spectrum apeared in the corresponding experimental ones measured by Ting *et al.* and Sheps, while the action spectrum measured by Beames *et al.* shows no vibronic structure (see below).

In the experimental work of Foreman *et al.*,[22] a high resolution of the absorption spectrum ($\lambda > 360$ nm) was reported and vibrational progressions were identified. The authors attributed

Fig. 8 The $B^1A' \leftarrow X^1A'$ absorption spectrum (with no dephasing time) using the uncoupled 1D, 2D and 3D Hamiltonian models in CH_2OO molecule. Spectrum changes its feature below and above the barrier energies E_b 3.43, 3.80 and 4.20 eV within the 1D, 2D and 3D Hamiltonian models, respectively from quasi-discrete to continuous structure. Due to the small width (slow tunneling) the narrow spectral features look discrete to the eye.

20442 | *Phys. Chem. Chem. Phys.*, 2025, **27**, 20433–20452

This journal is © the Owner Societies 2025

These continuous and quasi-discrete features of the spectrum can be understood by looking at the behavior of WP at the barrier energy. The WP is partly reflected by the barrier to the right of the shallow well (at ~ 1.7) resulting in the discrete structure in the spectrum as shown in the lower panel of Fig. 16. Some parts of the WPs penetrate the barrier (by tunneling) and reach the CAP, which is activated at $R_{OO} \sim 2.11$ (after the barrier of the diabatic B state potential energy curve, shown in Fig. 5). This part of the WP is absorbed in the CAP resulting in a different spectral feature, namely a small width of the quasi-discrete structures below the barrier and an continuous structure above the barrier.

5.2 $(CH_3)_2COO$

The $B^1A'-X^1A'$ absorption spectrum $(CH_3)_2COO$ was measured by Peltola *et al.* within the wavelength range of 320–340 nm.[63] The spectrum shows clearly strong oscillatory structures in this wavelength range, which have not been detected in the other experimental results (see for *e.g.* ref. 64).

In ref. 32, we studied the $B^1A' \leftarrow X^1A'$ absorption spectrum using the nuclear qunatum dynamics approach. The 3D PESs were obtained by employing the RS2C method as mentioned in Section 4. Similar to CH_2OO, we used the relaxation scheme to compute the initial wavepacket corresponding to the ground state PESs. Then, we lift the wavepacket from ground state to the excited state B^1A' in the propagation calculation. The computed spectrum (using the 3D coupled Hamiltonian model) is shown in Fig. 9 (shown by the solid red line) and compared with the experimental recording taken from ref. 64 (shown by
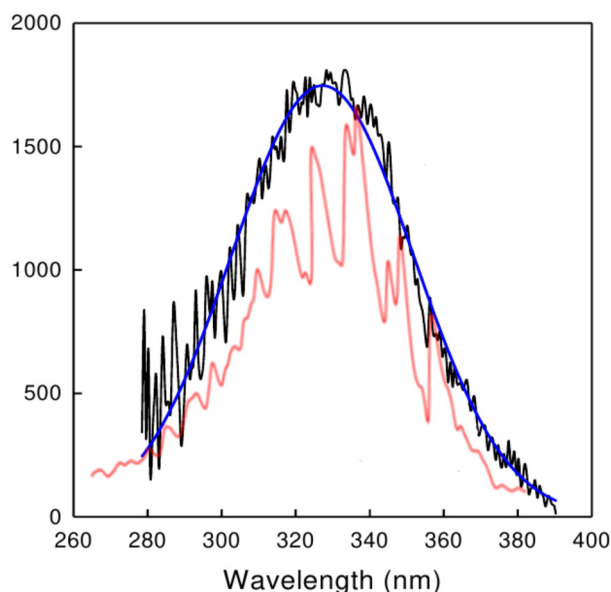
the solid black and blue lines). The agreement between theory and experiment is satisfactory; oscillatory structures rather than noise can be seen in both computed and measured spectrum, the width of the experimental and theoretical spectra is quite similar and finally the main peak of the computed spectrum is 328 nm compared to the experimental value (330 nm).[9,28,64] Peltola *et al.* obtained a value of 340 nm for the main peak of the $B^1A'-X^1A'$ absorption spectrum.[63]

In Fig. 10, we present the spectrum with no phenomenological dephasing time in the wavelength range of 400–320 nm (shown by the red line) using the coupled 3D model.[32] In this figure, the computed spectrum is compared with the measured spectrum of Peltola *et al.*[63] represented by the blue line. It can be seen that the simulation can generate the spectrum with strong oscillatory structures similar to what is observed in the experiment. The locations of stong peaks in both theory and experiment are reasonably close to each other, except for peaks located beyond 370 nm in the spectrum. As observed for CH_2OO, where its photodissociation occurs upon the B–X electronic excitation,[31] $(CH_3)_2COO$ upon electronic excitation from 280 to 400 nm undergoes rapid dissociation due to the repulsive PES of the excited B state. At the lowest dissociation asymptote, the photolysis products are $(CH_3)_2CO + O(^1D)$.
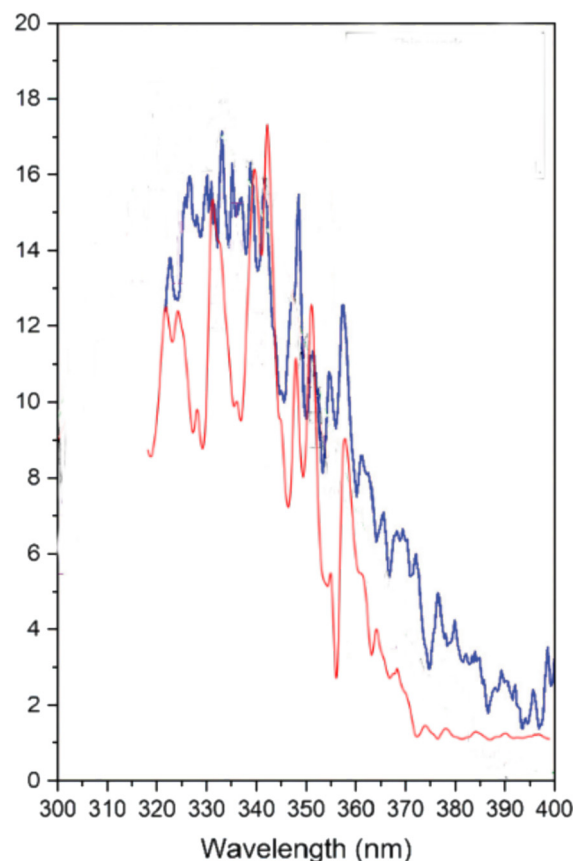
Fig. 9 The computed $B^1A'-X^1A'$ absorption spectrum of $(CH_3)_2COO$ using the coupled 3D model (shown by red line with dephasing time, $\tau = 25$ fs) compared with the available experimental spectrum (shown by black and blue lines) taken from ref. 64. The computed spectrum is obtained by employing the coupled 3D model depending the stretching modes R_{OO}, R_{CO} and the bending mode θ_{COO}.

Fig. 10 The computed $B^1A'-X^1A'$ absorption spectrum of $(CH_3)_2COO$ using the coupled 3D model (shown by red line with no dephasing time) compared with a high resolution experimental spectrum (shown by blue line) taken from ref. 63.
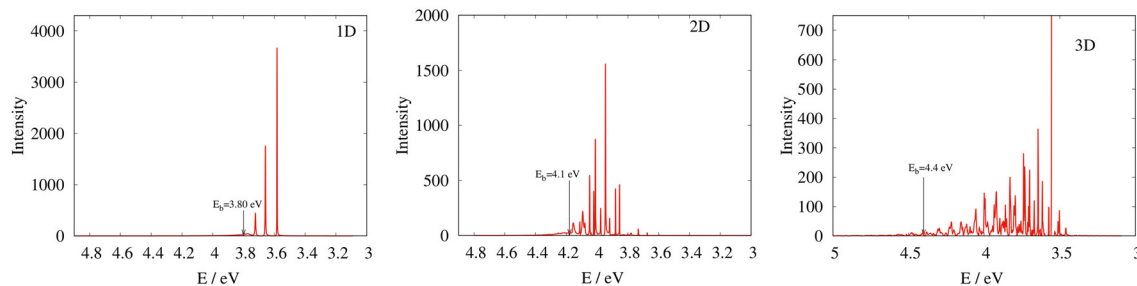
This journal is © the Owner Societies 2025

Phys. Chem. Chem. Phys., 2025, **27**, 20433–20452 | **20443**

Fig. 11 The B^{1}A′ ← X^{1}A′ absorption spectrum (with no dephasing time) using the uncoupled 1D, 2D and 3D Hamiltonian models in (CH$_3$)$_2$COO molecule. Spectrum changes its feature below and above the barrier energies E_b 3.80, 4.1 and 4.40 eV within the 1D, 2D and 3D Hamiltonian models, respectively from quasi-discrete to continuous structure.

Similar to CH$_2$OO, we want to investigate the role of vibronic coupling in generating spectrum and photodissociation dynamics. For this task, we compute spectrum using uncoupled 1D, 2D and 3D Hamiltonian models. The corresponding results are shown in Fig. 11. Comparing the spectrum computed by the uncoupled 3D Hamiltonian model in Fig. 11 with the spectrum computed with the coupled 3D Hamiltonian model in Fig. 9 leads us the conclusion that the vibronic coupling plays an important role in the absorption spectrum, while this was less the case for CH$_2$OO. For this molecule, we can see that the spectrum has continuous and quasi-discrete features above and below the barrier energy, respectively, for spectra computed using the 1D, 2D and 3D Hamiltonian models. Furthermore, Fig. 11 reveals that the barrier energy moves toward to the high-energy part of the absorption spectrum, when we enhance the dimensionality of the Hamiltonian model, similar to CH$_2$OO. The continuum part of spectrum goes to the spectral tail (above barrier energy of 4.4 eV). Most parts of the spectrum remain below the energy barrier within the uncoupled 3D model, so that it shows a quasi-discrete structur (also observed in CH$_2$OO). For understanding the continuous and quasi-discrete features of the spectrum in this molecule, the same argument mentioned for CH$_2$OO holds. In other words, some parts of the WP are reflected by the barrier resulting in the quasi-discrete structure in the spectrum (shown in the upper panel of Fig. 16).

Other parts of the WPs penetrate the barrier by tunneling and reach the CAP, which is activated at $R_{OO} \sim 2.11$, shown in Fig. 5.

5.3 CH$_3$CH$_2$CHOO

As shown in Fig. 1, this molecule has two conformers which are termed as *syn*- and *anti*- CH$_3$CH$_2$CHOO conformers. The experimental absorption spectroscopy for CH$_3$CH$_2$CHOO was carried out nearly a decade ago.[28] This relatively large Criegee intermediate was photolytically generated from diiodo precursors, detected by VUV photoionization at 118 nm, and spectroscopically characterized *via* UV-induced depletion of the $m/z = 74$ signals under jet-cooled conditions.[28] As a result, the strong UV absorption assigned to the B^{1}A′ ← X^{1}A′ transition with π* ← π character and peaked at 320 nm was measured within wavelength window 280–440 nm.[28]

In ref. 33, we conducted a nuclear quantum dynamical study relying on the 3D PESs computed by using the RS2C methods for each conformer as mentioned in Section 4. Similar to other Criegee intermediates, we used the relaxation scheme, computed the ground state wavefunction and lifted the ground state wavefunction to the excited B state in the propagation calculation. The propagation time was chosen to be 1000 fs with a time step of 0.5 fs.

The *syn*-, *anti*- as well as the cumulative spectra of CH$_3$CH$_2$CHOO employing the coupled 3D model with the
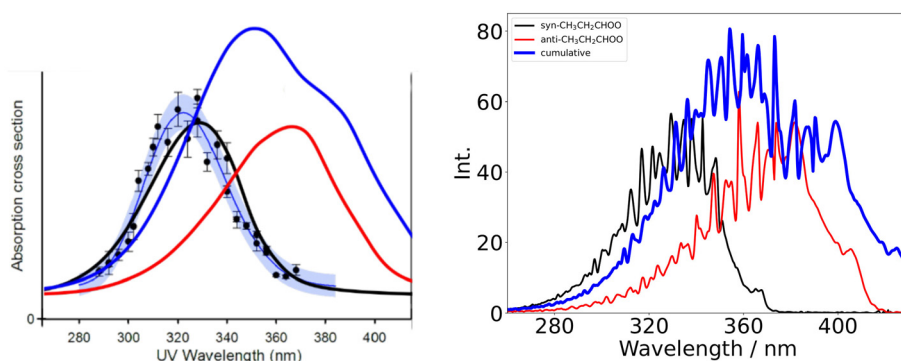

Fig. 12 The computed B^{1}A′ ← X^{1}A′ absorption spectrum of CH$_3$CH$_2$CHOO using the coupled 3D model for the two conformers *syn*- and *anti*- shown by black and red lines with dephasing time (left panel) τ = 10 fs, which is compared with the experimental absorption spectrum (black points) of CH$_3$CH$_2$CHOO taken from ref. 28. The spectra for both conformers with no dephasing time are shown in the right panel. The cumulative spectrum shown by a bold blue line.

20444 | *Phys. Chem. Chem. Phys.*, 2025, **27**, 20433–20452

This journal is © the Owner Societies 2025

dephasing time 10 fs and no dephasing time in the left and and right panels of Fig. 12. As can be seen in this figure, we use the following color coding for the spectra; the black, red and blue lines are for *syn-*, *anti-* and the cumulative spectra, respectively. In the left panel of Fig. 12, we compared our result with

experiment shown by black dots taken from ref. 28. The cumulative spectrum, which is the sum over the spectra of each conformer, is computed assuming that the excitation to the B state from the ground state X takes place with the same probability for both conformers.
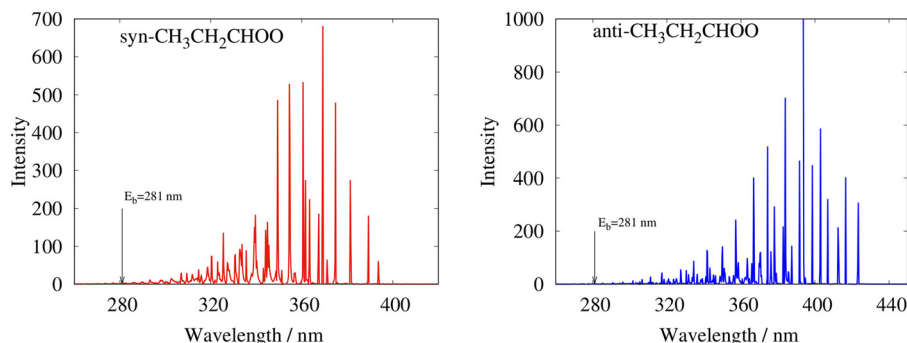
Fig. 13 The $B^1A' \leftarrow X^1A'$ absorption spectrum (with no dephasing time) using the uncoupled 3D Hamiltonian models in *syn-* and *anti-*CH_3CH_2CHOO conformers. Spectrum changes its feature below and above the barrier energy E_b 4.40 eV within this model from quasi-discrete to continuous structure.
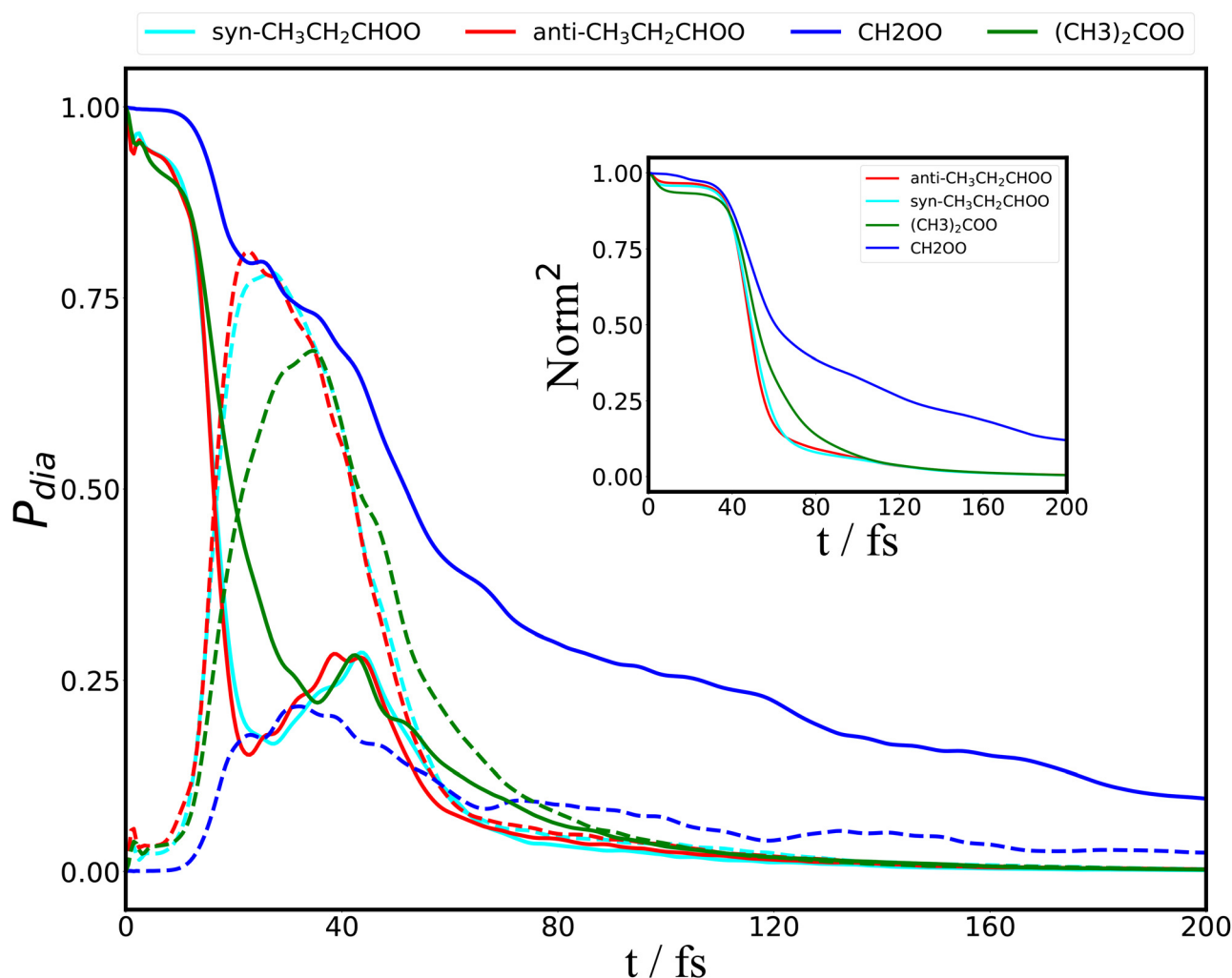
Fig. 14 The diabatic populations of the B^1A' and C^1A' states for the *syn-* and *anti-*CH_3CH_2CHOO, $(CH_3)_2COO$ as well as CH_2OO. For all molecules, we use the 3D coupled model Hamiltonian. The populations of the B and C states are shown by the solid and dashed lines, respectively.

This journal is © the Owner Societies 2025

Phys. Chem. Chem. Phys., 2025, **27**, 20433–20452 | **20445**

Comparing the computed spectrum with the experiment indicates that the spectrum obtained from *syn-* conformer is very close to the experimental spectrum in the left panel of Fig. 12 taken from ref. 28. As a consequence, the spectrum measured in ref. 28 may be attributed to the $B^1A' \leftarrow X^1A'$ transition of the *syn-* conformer. In Fig. 12, the spectrum shown by a red line is assigned to the $B^1A' \leftarrow X^1A'$ transition for the *anti*-conformer.

For CH_3CHOO molecule, experimentally and theoretically separate spectra of the two possible structural isomers were suggested.[65,66] Sheps *et al.* were able to detect the distinct spectra of the two conformers using their different reactivity towards H_2O and SO_2.[65] As a consequence, it was found that the spectra of the two conformers are enough separated to allow direct conformer-specific probing of the reactions of CH_3CHOO with other important tropospheric species.[65] Furthermore, it was shown that *syn*-CH_3CHOO peaks at the shorter wavelength range of the absorption spectrum, while the peak of *anti*-CH_3CHOO is located in the longer wavelength

range of the spectrum. We also reported similar observation for CH_3CH_2CHOO in ref. 33, where the *syn-* and *anti*-CH_3CH_2CHOO conformers are sufficiently separated; the band maximum of the *syn*-conformer spectrum (the black line in Fig. 12) is moved toward higher energy, while the band maximum of the *anti*-conformer spectrum is at the low energy side of the spectrum (red-shifted from *syn*-CH_3CH_2CHOO absorption).

In the following, we recalculate the absorption spectra for these conformers using the 3D model Hamiltonian ignoring the vibronic coupling between the B and C states (the uncoupled Hamiltonian model). The corresponding results are shown in Fig. 13. It can be seen that the prominent features are quasi-discrete though irregular line structures in Fig. 13, which are replaced by broad peaks in the right panel of Fig. 12, due to the coupling to the lower, repulsive energy surface (seen in Fig. 2 and 5). Thus, one infers that the vibronic coupling is essential for the Hamiltonian model to correctly produce the relevant physical observables, especially in the larger Criegee
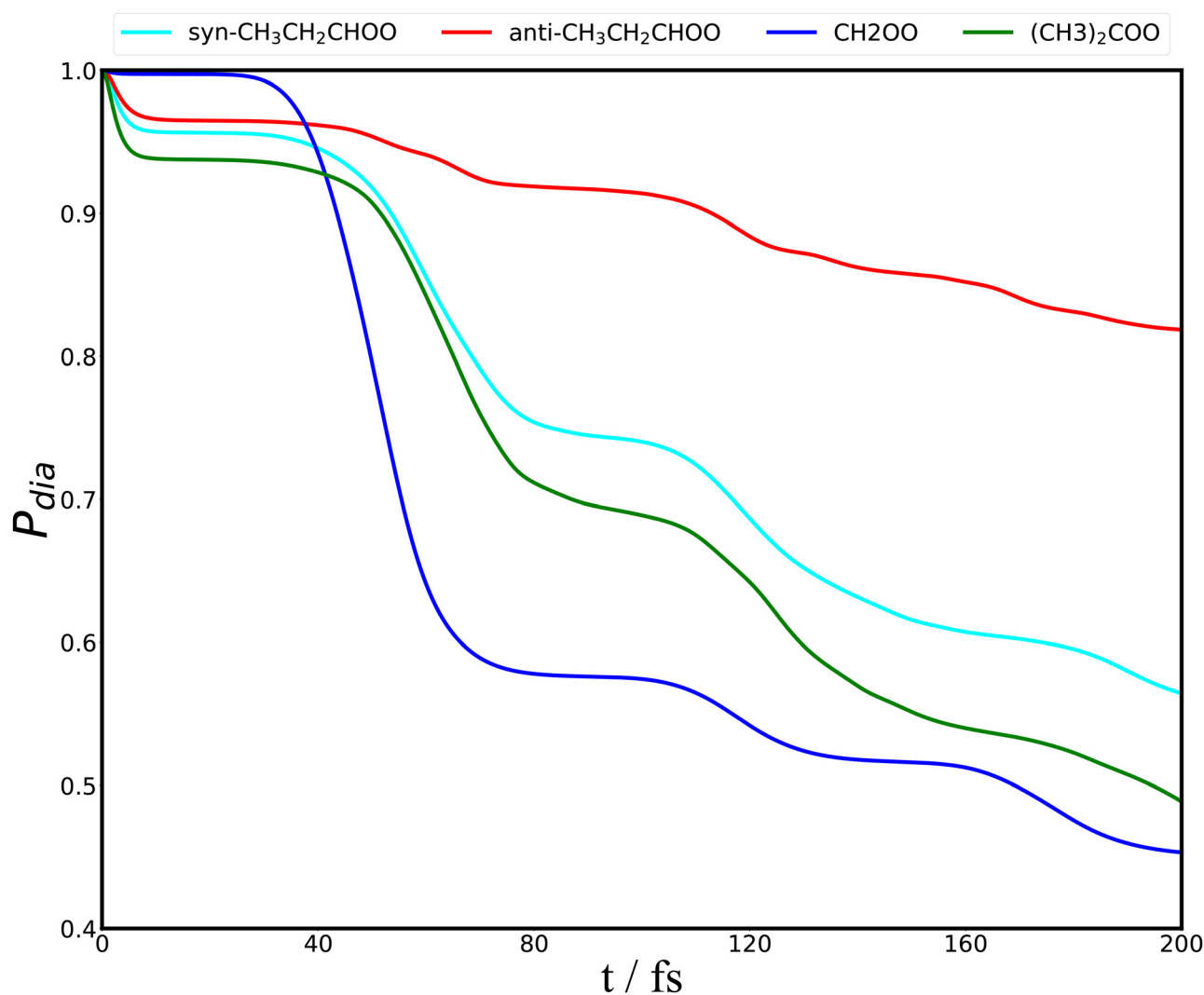

Fig. 15 The diabatic populations of the B^1A' state or squared norm for the *syn-* and *anti*-CH_3CH_2CHOO, $(CH_3)_2COO$ as well as CH_2OO. We use the 3D uncoupled model Hamiltonian.

20446 | *Phys. Chem. Chem. Phys.*, 2025, **27**, 20433–20452

This journal is © the Owner Societies 2025

intermediates as opposed to the smallest Criegee intermediate CH_2OO.

6 Time-dependent quantities

We calculate the time-dependent populations of the B and C states in the diabatic representation of eqn (6). As indicated in the previous section, employing the wavepacket propagation method results in the nuclear wavefunction $\Psi_\alpha(t)$ describing the nuclear quantum dynamics of a molecular system composed of several electronic states and f nuclear degrees of freedom.[34–36] For the Criegee intermediates studied in this work, we choose three nuclear degrees of freedom ($f = 3$), which are the O–O and C–O stretching and C–O–O bending modes. For each molecule, the diabatic electronic populations $P_\alpha(t)$ (with α being B or C state in our case) can be computed as $\langle \Psi_\alpha(t) | \Psi_\alpha(t) \rangle$.[35]

In Fig. 14, the diabatic populations of the B and C states for the Criegee intermediates are presented.[31–33] At $t = 0$, the populations of the diabatic B and C states in each molecule are one and zero, respectively, because the B state is populated by lifting wavepacket from the ground to the B state in the propagation calculation. At a time of ~ 20 fs, there is a rapid and efficient transfer of B state population to the C state for *syn*, *anti* conformers and $(CH_3)_2COO$, while for CH_2OO, the population transfer is moderately slower than for the larger Criegee intermediates. In the inset of Fig. 14, the squared norm of the wavepacket within the 3D model Hamiltonian is also shown for each molecule. It can be concluded that also the norm of the wavepacket in CH_2OO initially decays slowly compared to the other, larger Criegee intermediates. In Fig. 15, the diabatic populations of the B state for the relevant molecular systems are depicted by using the uncoupled Hamiltonian model. Comparing the norm of the wavepacket in Fig. 15 and the inset of Fig. 14 shows that the behavior of the norm within the
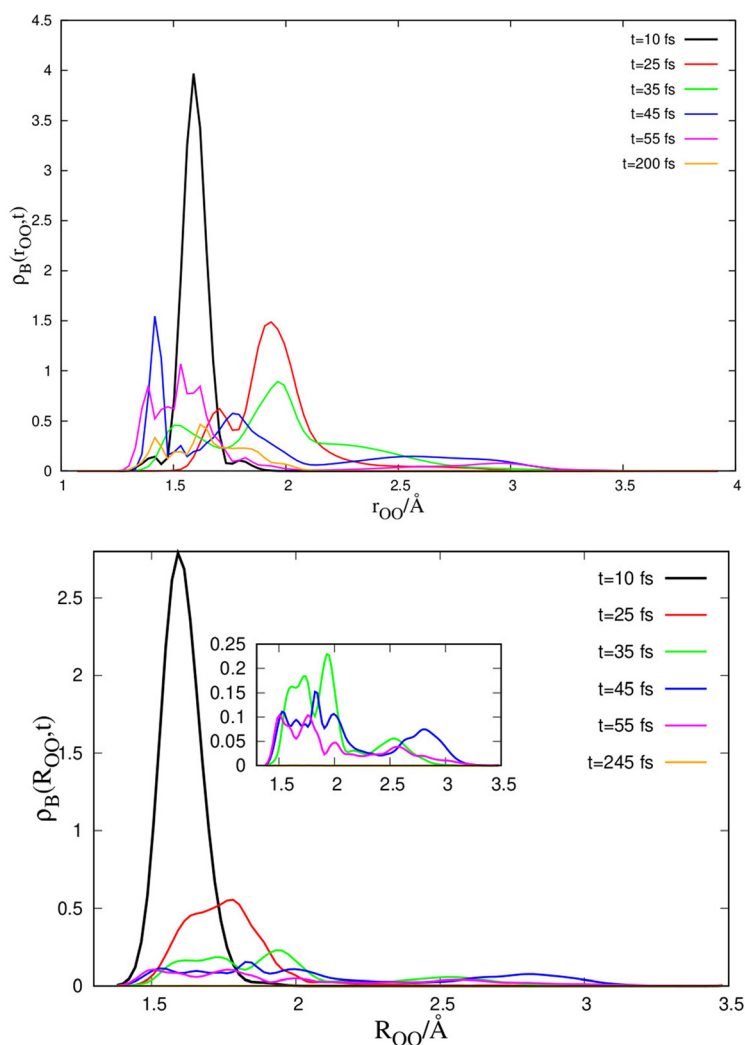
Fig. 16 One-dimensional reduced densities for the B state of CH_2OO (upper panel) and $(CH_3)_2COO$ (lower panel). Conformers along R_{OO} are computed using the coupled 3D model. In the inset of the upper panel, we zoom in on the one-dimensional reduced densities for $t > 25$ fs, where the WP reaches the CAP.

This journal is © the Owner Societies 2025

Phys. Chem. Chem. Phys., 2025, **27**, 20433–20452 | **20447**

these molecular species. To address it, we set up a nuclear quantum dynamical mechanisms such as calculation for CH_2OO in ref. 38 and included the triplet states a^3A', b^3A', a^3A'' and b^3A'' in our calculation. As spin–orbit couplings (SOC) between the singlet and the triplet states are taken into account, PESs of triplet states with different spin components $M_s = 0, \pm1$ and their SOCs with the other singlet states B and C are explicitly treated in the Hamiltonian model.[38] In Fig. 19, the potential energy cuts for the aforementioned triplet and singlet states are shown, where we use the RS2C-F12 method with cc-pVTZ-F12 basis set for all atoms. From this figure, several avoided crossings can be observed between the PE curves of the excited singlet and triplet states with the same symmetry. As shown in the lower panel of Fig. 19, avoided crossings occur between the two singlet states B^1A' and C^1A' at 3.06 eV with $R_{OO} = 1.741$, between the excited triplet states a^3A' and b^3A' at 2.35 eV with $R_{OO} = 1.591$ and finally between the excited triplet states a^3A'' and b^3A'' at 2.57 eV with $R_{OO} = 1.591$. The dissociation channel along the O–O stretching coordinate after excitation to the B state leads to the $H_2CO(X^1A_1)$ and O^1D products. The electronic states X^1A', B^1A' and C^1A' correlate with this same asymptotic limit generating the $H_2CO(X^1A_1)$ and O^1D products as shown in the upper panel of Fig. 19. The dissociation energy for this channel is estimated to be ≈ 57 kcal mol^{-1} or 2.47 eV, which is in close agreement with the experimental value ≈ 54 kcal mol^{-1} or 2.34 eV.[67] In the upper panel of Fig. 19, the three triplet states a^3A', a^3A'' and b^3A'' correlate adiabatically with the same state in the asymptotic O–O stretching region and this represents a dissociation channel, which is energetically lower than the aforementioned dissociation channel. In this new channel, $CH_2OO(X^1A')$ is dissociated into $H_2CO(X^1A_1)$ and O^3P products. As shown in ref. 38, the dissociation energy attributed to this channel is estimated as ≈ 13 kcal mol^{-1} or 0.56 eV.

For the purpose of the dynamics, we diabatized PESs and SOCs matrix elements which are primarily evaluated within the adiabatic picture.[38] In principle, the diabatization is one way to incorporate PESs and SOCs data allowing to describe both IC and ISC using a fully quantal approach.[38] The advantage of using PESs and SOC matrices in the diabatic picture is to remove not only the singular derivative couplings and discontinuities appearing in PESs (owing to the presence of avoided crossings in the adiabatic picture) but also the discontinuities in SOCs as a function of the nuclear coordinates. Based on the 3D PESs including SOCs (in the diabatic picture), the spectrum in the energy range below 2.8 eV was computed in ref. 38. This spectral band is due to contributions of the two lowest triplet states with a^3A' and a^3A'' symmetry including their SOCs with the B^1A' and C^1A' states. As shown in that reference, the spectral band shows an irregular and discrete structure which is ~ 0.9 eV above the minimum energy of the 3D PESs of a^3A' ($E_{min} = 1.45$ eV). Furthermore, this spectral band is below the energy barrier of the a^3A'' state (3.09 eV). In ref. 60, the dynamics of the the triplet states of Criegee intermediates using trajectory surface-hopping (TSH) molecular dynamics simulations was reported. However, they could not observe any population transfer to the triplet states in their calculation even for large Criegee intermediates. Our finding in ref. 38 shows that there is a population transfer among triplet and singlet states. Thus, it is required to consider the triplet states to capture correct photodissociation dynamics for all Criegee intermediates. Our finding is aligned with other findings for molecular systems with a similar size to formaldehyde oxide, such as formaldehyde and acetaldehyde,[68] wherein photodissociation is driven by eventual formation of a triplet state manifold mediated by efficient intersystem crossing from an initially excited bright singlet state. Van veen *et al.* reported the
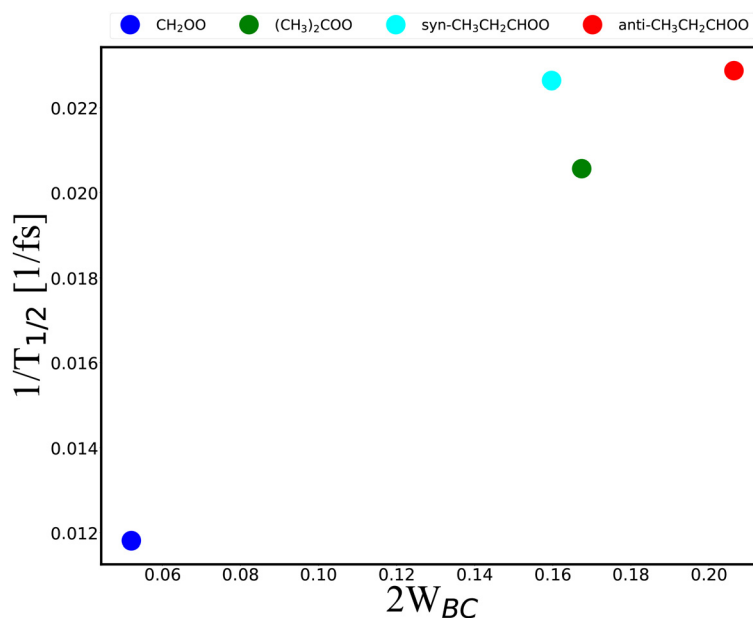

Fig. 18   The inverse lifetime are plotted against twice the vibronic coupling W_{BC} for the Criegee intermediates.

This journal is © the Owner Societies 2025

Phys. Chem. Chem. Phys., 2025, **27**, 20433–20452 | **20449**

absorption spectra of formaldehyde and acetaldehyde including spectral bands with important contributions from the lowest triplet states and possible SOCs between the singlet and triplet states in these aldehydes.[68]

As explained here and in ref. 38, the contributions of the triplet states and the spin–orbit couplings (SOCs) between relevant singlet and triplet states are crucial for accurately capturing the photodissociation dynamics of CH_2OO. The same reasoning applies to larger Criegee intermediates, where we believe that the involvement of triplet states and their SOCs with several low-lying singlet states will offer valuable insight into the various photodissociation pathways.
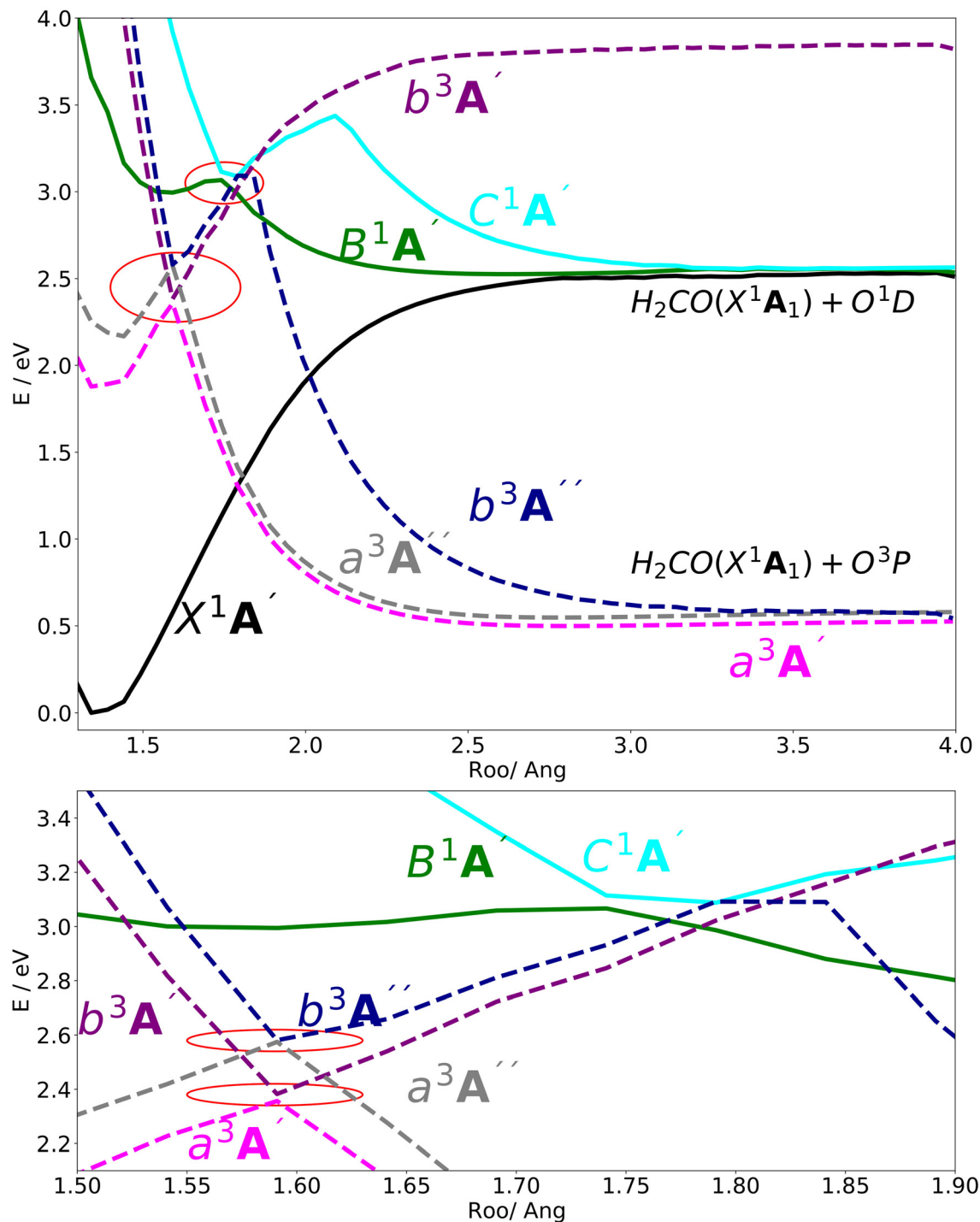
Fig. 19 (Upper) the adiabatic PE curves along the OO stretching mode for the X^1A', B^1A', C^1A', a^3A', b^3A', a^3A'' and b^3A'' states. (Lower) the adiabatic PE curves along O−O stretching mode, zooming in geometries in the range $1.55 < R_{OO} < 1.80$ (indicated by red circles in the upper panel). The bonding angle θ_{COO} and the stretching mode R_{CO} are fixed at the equilibrium structure values 117.905° and 1.27, respectively.

20450 | *Phys. Chem. Chem. Phys.*, 2025, **27**, 20433–20452

This journal is © the Owner Societies 2025

8 Concluding remarks

In this article we have surveyed salient features of some representative Criegee intermediates, the parent system CH_2OO and three alkyl derivatives with two carbon atoms in the alkyl moiety (*i.e.* not counting the parent-system C-atom, see Fig. 1). These species share important joint features, in particular a rapid O–O bond cleavage in the presence of UV light accompanied by a broad and partly structureless spectral band in the 280–400 nm wavelength range. Further joint features are femtosecond internal conversion processes caused by the near-degenerate B and C excited states, leading to a rapid population transfer between the singlet states (for the triplet states see the remark below). Nevertheless also important differences deserve mentioning.

The B–C energetic proximity differs substantially between the systems treated here, the gap being smallest (0.05 eV) for the parent system and considerably larger (0.18 eV) for the alkyl derivatives, see Fig. 4b. This impacts on the stability of these species as evidenced by the norm of the wavepacket (see inset of Fig. 14). After the rapid (incomplete) decay at 20–50 fs, the norm and B-state population of the parent system CH_2OO evolve more slowly than those of the larger systems because the asymptotic regime (with O–O dissociation being complete) is less easily accessible, see panels of Fig. 2. This is made more quantitative in CH_2OO Fig. 18 in which the lifetime is plotted against the vibronic coupling $2W_{BC}$, estimated as the avoided crossing energy gap according to Section IV. An interesting correlation is evidenced, which is nearly linear with the exception of *syn*-CH_3CH_2CHOO, to be analysed more deeply in future works. In particular, we have confirmed for the first time the presence of vibrational structures in the absorption spectra of both CH_2OO and $(CH_3)_2COO$ molecules (as shown in Fig. 7 and 10), which are consistent with the reported experimental spectra. These accurate computational results allow us to conclude that the dominant vibrational modes responsible for the observed features are the O–O and C–O stretching modes, as well as the C–O–O bending mode. Another important finding concerns the simulation of absorption spectra for different conformers of CH_3CH_2CHOO shown in Fig. 12. Our results indicate that the spectrum reported in ref. 28 should in fact be assigned explicitly to the *syn*-CH_3CH_2CHOO conformer- a novel assignment not previously recognized in the literature.

In a more complete study also spin–orbit coupling and spin-forbidden processes should be considered. So far this has been done for CH_2OO[38] and sometimes on a classical dynamical (SHT) level only[69] and was pointed out to lead to new, lower-energy disscociation channels.[38,69] In combination with the present approach it will allow for a unified description of spectral features and nonradiative phenomena in these systems in a broad sense.

Finally, in this work we have attempted to achieve a balanced accuracy for the different system sizes treated. If this can be achieved also for larger systems, for example with three or four C-atoms in the alkyl moiety, this is hoped to lay the ground for a comprehensive understanding of these elusive species.

Conflicts of interest

There are no conflicts of interest to declare.

Data availability

All raw data used in this review are available from the corresponding author upon reasonable request.

Acknowledgements

Notes and references

1 C. A. Taatjes, D. E. Shallcross and C. J. Percival, *Phys. Chem. Chem. Phys.*, 2014, **16**, 1704–1718.

2 R. Criegee, *Angew. Chem., Int. Ed. Engl.*, 1975, **14**, 745–752.

3 D. Johnson and G. Marston, *Chem. Soc. Rev.*, 2008, **37**, 699–716.

4 L. Vereecken and J. S. Francisco, *Chem. Soc. Rev.*, 2012, **41**, 6259–6293.

5 S. D. Piccot, J. J. Watson and J. W. Jones, *J. Geophys. Res.: Atmos.*, 1992, **97**, 9897–9912.

6 N. M. Donahue, G. T. Drozd, S. A. Epstein, A. A. Presto and J. H. Kroll, *Phys. Chem. Chem. Phys.*, 2011, **13**, 10848–10857.

7 A. Guenther, C. N. Hewitt, D. Erickson, R. Fall, C. Geron, T. Graedel, P. Harley, L. Klinger, M. Lerdau, W. A. Mckay, T. Pierce, B. Scholes, R. Steinbrecher, R. Tallamraju, J. Taylor and P. Zimmerman, *J. Geophys. Res.:Atmos.*, 1995, **100**, 8873–8892.

8 S. E. Paulson, M. Y. Chung and A. S. Hasson, *J. Phys. Chem. A*, 1999, **103**, 8125–8138.

9 H.-L. Huang, W. Chao and J. J.-M. Lin, *Proc. Natl. Acad. Sci. U. S. A.*, 2015, **112**, 10857–10862.

10 B. Long, J. L. Bao and D. G. Truhlar, *J. Am. Chem. Soc.*, 2016, **138**, 14409–14422.

11 Y.-T. Su, H.-Y. Lin, R. Putikam, H. Matsui, M. C. Lin and Y.-P. Lee, *Nat. Chem.*, 2014, **6**, 477–483.

12 L. Vereecken, H. Harder and A. Novelli, *Phys. Chem. Chem. Phys.*, 2014, **16**, 4039–4049.

13 L. Vereecken, H. Harder and A. Novelli, *Phys. Chem. Chem. Phys.*, 2012, **14**, 14682–14695.

14 Z. J. Buras, R. M. I. Elsamra, A. Jalan, J. E. Middaugh and W. H. Green, *J. Phys. Chem. A*, 2014, **118**, 1997–2006.

15 O. Welz, J. D. Savee, D. L. Osborn, S. S. Vasu, C. J. Percival, D. E. Shallcross and C. A. Taatjes, *Science*, 2012, **335**, 204–207.

16 C. A. Taatjes, G. Meloni, T. M. Selby, A. J. Trevitt, D. L. Osborn, C. J. Percival and D. E. Shallcross, *J. Am. Chem. Soc.*, 2008, **130**, 11883–11885.

This journal is © the Owner Societies 2025

Phys. Chem. Chem. Phys., 2025, **27**, 20433–20452 | **20451**

17 D. Johnson and G. Marston, *Chem. Soc. Rev.*, 2008, **37**, 699–716.

18 P. Rafaj, I. Bertok, J. Cofala and W. Schöpp, *Atmos. Environ.*, 2013, **79**, 472–479.

19 M. Nakajima and Y. Endo, *J. Chem. Phys.*, 2013, **139**, 101103.

20 J. M. Beames, F. Liu, L. Lu and M. I. Lester, *J. Am. Chem. Soc.*, 2012, **134**, 20045–20048.

21 L. Sheps, *J. Phys. Chem. Lett.*, 2013, **4**, 4201–4205.

22 E. S. Foreman, K. M. Kapnas, Y. Jou, J. Kalinowski, D. Feng, R. B. Gerber and C. Murray, *Phys. Chem. Chem. Phys.*, 2015, **17**, 32539–32546.

23 W.-L. Ting, Y.-H. Chen, W. Chao, M. C. Smith and J. J.-M. Lin, *Phys. Chem. Chem. Phys.*, 2014, **16**, 10438–10443.

24 J. M. Beames, F. Liu, L. Lu and M. I. Lester, *J. Chem. Phys.*, 2013, **138**, 244307.

25 E. P. F. Lee, D. K. W. Mok, D. E. Shallcross, C. J. Percival, D. L. Osborn, C. A. Taatjes and J. M. Dyke, *Chem. – Eur. J.*, 2012, **18**, 12411–12423.

26 R. Dawes, B. Jiang and H. Guo, *J. Am. Chem. Soc.*, 2015, **137**, 50–53.

27 R. Chhantyal-Pun, A. Davey, D. E. Shallcross, C. J. Percival and A. J. Orr-Ewing, *Phys. Chem. Chem. Phys.*, 2015, **17**, 3617–3626.

28 F. Liu, J. M. Beames, A. M. Green and M. I. Lester, *J. Phys. Chem. A*, 2014, **118**, 2298–2306.

29 Y.-Y. Wang, C.-Y. Chung and Y.-P. Lee, *J. Chem. Phys.*, 2016, **145**, 154303.

30 B. Nikoobakht and H. Köppel, *Mol. Phys.*, 2021, e1958019.

31 B. Nikoobakht and H. Köppel, *Phys. Chem. Chem. Phys.*, 2022, **24**, 12433–12441.

32 B. Nikoobakht and H. Köppel, *Phys. Chem. Chem. Phys.*, 2023, **25**, 19470–19480.

33 B. Nikoobakht and H. Köppel, *Chem. Phys. Lett.*, 2023, **833**, 140943.

34 M. Beck, A. Jäckle, G. Worth and H.-D. Meyer, MCTDH, The Heidelberg MCTDH Package Version 8.4.20, For the current version, see **https://www.pci.uni-heidelberg.de/tc/usr/mctdh/doc/index.html**.

35 M. Beck, A. Jäckle, G. Worth and H.-D. Meyer, *Phys. Rep.*, 2000, **324**, 1–105.

36 H.-D. Meyer, F. Gatti and G. Worth, *Multidimensional Quantum Dynamics: MCTDH Theory and Applications*, WILEY-VCH Verlag GmbH and Co. KGaA, Weinheim, 2009.

37 W. Domcke, D. R. Yarkony and H. Köppel, *Conical Intersections: Electronic Structure, Dynamics and Spectroscopy*, World Scientific, New Jersey, 2004.

38 B. Nikoobakht and H. Köppel, *Phys. Chem. Chem. Phys.*, 2024, **26**, 24591–24606.

39 H. Köppel, W. Domcke and L. S. Cederbaum, *Adv. Chem. Phys.*, 1984, **57**, 59–246.

40 C. Leforestier and R. E. Wyatt, *J. Chem. Phys.*, 1983, **78**, 2334–2344.

41 R. Kosloff and D. Kosloff, *J. Comput. Phys.*, 1986, **63**, 363–376.

42 U. V. Riss and H. Meyer, *J. Chem. Phys.*, 1996, **105**, 1409–1419.

43 E. B. Wilson, J. C. Decius and P. Cross, *Molecular vibrations: the theory of infrared and Raman vibrational spectra*, McGraw-Hill, New York City, 1955.

44 E. B. Wilson, *J. Chem. Phys.*, 1939, **7**, 1047–1052.

45 A. Jaeckle and H. Meyer, *J. Chem. Phys.*, 1996, **104**, 7974–7984.

46 G. Herzberg, *Molecular spectra and molecular structure. Electronic spectra and electronic structure of polyatomic molecules*, R.E. Krieger Pub. Co., Malabar, Fla., Florida, 1991, vol. 3.

47 E. Stueckelberg, *Helv. Chim. Acta*, 1932, **5**, 369.

48 C. Zener, *Proc. R. Soc. London*, 1932, **137**, 696.

49 H. Köppel, L. S. Cederbaum and W. Domcke, *J. Chem. Phys.*, 1982, **77**, 2014–2022.

50 H. Köppel, J. Gronki and S. Mahapatra, *J. Chem. Phys.*, 2001, **115**, 2377–2388.

51 H. Köppel and B. Schubert, *Mol. Phys.*, 2006, **104**, 1069–1079.

52 T. Shiozaki and H.-J. Werner, *J. Chem. Phys.*, 2010, **133**, 141103.

53 T. H. Dunning, *J. Chem. Phys.*, 1989, **90**, 1007–1023.

54 A. D. Becke, *J. Chem. Phys.*, 1993, **98**, 5648–5652.

55 P. J. Stephens, F. J. Devlin, C. F. Chabalowski and M. J. Frisch, *J. Phys. Chem.*, 1994, **98**, 11623–11627.

56 R. Krishnan, J. S. Binkley, R. Seeger and J. A. Pople, *J. Chem. Phys.*, 1980, **72**, 650–654.

57 P. Celani and H.-J. Werner, *J. Chem. Phys.*, 2000, **112**, 5546–5557.

58 T. Clark, J. Chandrasekhar, G. W. Spitznagel and P. V. R. Schleyer, *J. Comput. Chem.*, 1983, **4**, 294–301.

59 H.-J. Werner and P. Knowles, *MOLPRO, version 2019.2, a package of ab initio programs, For the current version*, see **https://www.molpro.net/**.

60 V. J. Esposito, O. Werba, S. A. Bush, B. Marchetti and T. N. V. Karsili, *Photochem. Photobiol.*, 2022, **98**, 763–772.

61 K. Takahashi, *J. Phys. Chem. A*, 2022, **126**, 6080–6090.

62 J. H. Lehman, H. Li, J. M. Beames and M. I. Lester, *J. Chem. Phys.*, 2013, **139**, 141103.

63 J. Peltola, P. Seal, N. Vuorio, P. Heinonen and A. Eskola, *Phys. Chem. Chem. Phys.*, 2022, **24**, 5211–5219.

64 Y.-P. Chang, C.-H. Chang, K. Takahashi and J. J.-M. Lin, *Chem. Phys. Lett.*, 2016, **653**, 155–160.

65 L. Sheps, A. M. Scully and K. Au, *Phys. Chem. Chem. Phys.*, 2014, **16**, 26701–26706.

66 J. C. McCoy, B. Marchetti, M. Thodika and T. N. V. Karsili, *J. Phys. Chem. A*, 2021, **125**, 4089–4097.

67 H. Li, Y. Fang, J. M. Beames and M. I. Lester, *J. Chem. Phys.*, 2015, **142**, 214312.

68 E. H. van Veen, W. L. van Dijk and H. H. Brongersma, *Chem. Phys.*, 1976, **16**, 337–345.

69 V. J. Esposito, T. Liu, G. Wang, A. Caracciolo, M. F. Vansco, B. Marchetti, T. N. V. Karsili and M. I. Lester, *J. Phys. Chem. A*, 2021, **125**, 6571–6579.

20452 | *Phys. Chem. Chem. Phys.*, 2025, **27**, 20433–20452

This journal is © the Owner Societies 2025